

Peer review status:

This is a non-peer-reviewed preprint submitted to EarthArXiv.

# Application of automatic differentiation to the inversion of nonlinear mantle rheology using plate motion and topography

Zhiying Ming<sup>1</sup>, Jiashun Hu<sup>1,2\*</sup>, Weiqiang Zhu<sup>3</sup>

<sup>1</sup> Department of Earth and Space Sciences, Southern University of Science and Technology, Shenzhen 518055, China

<sup>2</sup> Guangdong Provincial Key Laboratory of Geophysical High-resolution Imaging Technology, Southern University of Science and Technology, Shenzhen

<sup>3</sup> Department of Earth and Planetary Science, University of California, Berkeley, CA 94720, USA

3 May 2025

## SUMMARY

The rheological properties of the mantle govern plate tectonics and mantle convection, yet constraining the rheological parameters remains a significant challenge. Laboratory experiments are usually performed under different temperature-pressure-strain-rate conditions than those of natural environments, leading to substantial uncertainties when extrapolating the parameters to real-world conditions. While traditional Bayesian inversion with Monte Carlo sampling methods offers sufficient exploration of the parameter space and accurate inversion results, the excessive computational cost limits its practical application to complex nonlinear problems. To address these limitations, we integrate finite-difference-based geodynamic forward modeling with Automatic Differentiation (AD) to build a framework to invert non-linear rheological parameters. By incorporating multisource observational data, including surface velocities and topography, we are able to invert critical rheological parameters of the lithosphere and mantle, including the viscosity pre-exponential factor, activation energy, stress exponent, yield stress, and plate-interface viscosity. To validate the method, a series of models with different levels of complexity from single- to multiple-subduction systems and consideration of data noises are designed to generate synthetic data that are further used for inversion. Our method can successfully restore the rheological parameters under various conditions, with minimal errors between predicted and true values, underscoring its stability and broad applicability. In general, this study introduces a highly efficient and practical geodynamic forward and inverse modeling approach that can be used to infer the rheology of the mantle.

Key words: Automatic Differentiation; Stokes equations; Inverse Problem; Finite Difference Method; Geodynamics

## 1 INTRODUCTION

Plate tectonics and mantle dynamics govern the evolution of the solid Earth, with their long-term mechanical behavior ultimately controlled by mantle rheology (Ranalli, 1995; Karato, 2008). However, rheology is one of the least well-constrained physical properties of the solid Earth, leading to substantial debates surrounding the forces and deformation patterns of the internal Earth. For example, although it is well accepted that plate subduction is primarily driven by the gravitational potential energy of slabs and impeded by various types of energy dissipation, some studies have suggested that slab bending is the most important mechanism of energy dissipation (Conrad & Hager, 1999; Buffett & Rowley, 2006; Buffett, 2006), but others have derived a

much lower bending dissipation, generally less than 20% of the total gravitational potential energy (Capitanio et al., 2009; Leng & Zhong, 2010; Schellart, 2009). This ultimately depends on the viscosity of slab hinge. There have also been studies suggesting plate interface shearing as an important mechanism of energy dissipation, as evidenced by its strong influence on plate motion (Sobolev & Brown, 2019; Hu et al., 2024; Behr & Becker, 2018; Zhou et al., 2024) and exemplified by the abrupt increase of India-Eurasia convergence at 65 Ma due to the lubrication effect of Indian passive-margin sediment subduction (Zhou et al., 2024). A more quantitative estimate of the energy dissipation requires a better understanding of the viscoplastic behavior of the plate interface. There is also considerable debate on the peak amplitude of dynamic topography, which ranges from around 2 km (Yang & Gurnis, 2016; Steinberger, 2007; Lithgow-Bertelloni & Richards, 1998; Conrad & Husson, 2009; Fla-

\* Corresponding author: hujs@sustech.edu.cn

ment et al., 2013), to around 1 km (Yang et al., 2017; Davies et al., 2019), and even 0.5 km (Hoggard et al., 2016). This debate results from the large uncertainties on the viscosity of the underlying mantle. The viscosity of the mantle has also been a key concern for studies on plate driving forces with respect to the role of basal drag (Conrad & Lithgow-Bertelloni, 2002; Becker & Faccenna, 2011; Cui et al., 2024; Li et al., 2024b), on subducting slab morphology including the stagnation at  $\sim 660$  km and  $\sim 1000$  km depth (Goes et al., 2017; Li et al., 2019; Rudolph et al., 2015; Fei et al., 2023; Čížková & Bina, 2019), and on the morphology and stability (or mobility) of LLVP (Torsvik et al., 2008; McNamara & Zhong, 2005; Zhang et al., 2024; Shi et al., 2024), etc. Although there is an urgent need for a comprehensive understanding of mantle rheology, methods to constrain mantle rheology are still limited, and uncertainties of mantle rheology are still large.

The rheology of the mantle can be described by a number of deformation mechanisms, including diffusion creep, dislocation creep, Peierl’s creep and plasticity, with a number of rheological parameters (such as activation energy, stress exponent, and yield stress) defining their dependence on temperature, pressure, strain rate, grain size, and so on (Ranalli, 1995; Karato, 2008). In laboratory settings, the rheological parameters of rocks can be measured through high-temperature and high-pressure experiments (Karato & Wu, 1993; Hirth & Kohlstedt, 2003; Korenaga & Karato, 2008). These experimental results have been successfully applied in forward geodynamic modeling with realistic predictions of tectonic plates and mantle flow (Billen & Hirth, 2007; Behn et al., 2009; Stadler et al., 2010; Hu et al., 2022; Li et al., 2024a). However, laboratory conditions cannot fully replicate the complex environment of mantle rocks in the Earth’s mantle, particularly with regard to the relatively slow strain rate and high P-T condition. This limitation introduces significant uncertainties when extrapolating laboratory-derived parameters to real-world applications.

On the other hand, there are a range of observational data available on the Earth surface that can be used to invert mantle rheology, such as plate velocities (Becker & O’Connell, 2001; Forte et al., 1991; Wu et al., 2008; Hu et al., 2024), stress orientations (Reuber et al., 2020), gravity anomalies (Hager, 1984; Liu & Zhong, 2015; Rudolph et al., 2015; Steinberger & Calderwood, 2006), and topography including those that use post-glacial rebound (Baumann et al., 2014a; Cathles, 2015; Mitrovica & Forte, 2004). Although most studies using these observations were performed using forward geodynamic modeling, inversion methods are continuously developed to make the finding of best-fit parameters automatic. For example, Baumann et al. (2014a) and Baumann & Kaus (2015) constrained the lithospheric plate strength and nonlinear viscosity parameters by Bayesian inversion with surface velocity, Bouguer gravity anomalies, and topographic data. However, the Bayesian method requires substantial computational resources, on the order of tens of thousands or even hundreds of thousands of forward simulations to obtain the posterior probability distribution. To improve efficiency, adjoint method has been combined with Bayesian inversion for inferring lithospheric and mantle rheological parameters. By leveraging the adjoint method to compute gradients for parameter optimization (Ratnaswamy et al., 2015; Rudi et al., 2022; Bunge

et al., 2003; Horbach et al., 2014; Hu et al., 2024), the number of forward simulations is significantly reduced, greatly enhancing the efficiency of the inversion process. This eventually leads to the inversion of realistic nonlinear mantle viscosity on a global scale (Hu et al., 2024). However, the adjoint method also faces challenges such as complex mathematical derivations and the need to derive different adjoints for varying scenarios (Plessix, 2006). There are also studies that employed physics-informed neural networks (PINNs) to address the forward and inverse problems of partial differential equations (PDEs), particularly the Navier-Stokes equations (Raissi et al., 2019; Cai et al., 2021). Their work introduced a novel approach for solving and inverting nonlinear PDEs. However, the method still faces challenges in terms of transferability and interpretability.

In recent years, automatic differentiation (AD), widely used as a gradient computation method in the field of deep learning, has been introduced into the study of geophysical inverse problems (Paszke et al., 2017; Baydin et al., 2018). AD is an efficient method that computes derivatives based on the chain rule and has been widely applied in optimization, deep learning, and scientific computing. When calculating gradients, AD decomposes the target function into a series of simple computational units, constructs a computational graph, and utilizes the chain rule to automatically propagate gradients from output to input. Sambridge et al. (2007) highlighted the significant advantages of automatic differentiation in the field of Earth sciences, as it combines the physical interpretability of finite difference methods with the precision and efficiency of analytical derivatives. This approach has already been applied to various geophysical problems, including full-waveform inversion in seismology (Zhu et al., 2021, 2022; Liu et al., 2025). This gradient computation method has been mathematically proven to be equivalent to the adjoint method (LeCun et al., 1988), while offering superior accuracy, efficiency, and versatility, thereby providing a powerful new tool for parameter inversion in geodynamics.

Recent studies have also attempted to apply automatic differentiation (AD) to gradient computation in geodynamic inverse problems involving the Stokes equations. For example, the G-ADOPT framework, built upon Firedrake and Dolfin-Adjoint, enables adjoint-based optimization for large-scale, nonlinear mantle convection simulations (Ghelichkhan et al., 2024). Other approaches combine TAF (Transformation of Algorithms in Fortran) with community codes such as StagYY to obtain AD-based gradients (Coltice et al., 2023). By decomposing the discretized Stokes solver into a sequence of operators and applying automatic differentiation techniques, it becomes possible to compute accurate parameter sensitivities and enable efficient optimization strategies. In this study, we extend this idea by coupling the numerical solution of the Stokes equations with PyTorch’s automatic differentiation engine. This results in a flexible and modular framework that can seamlessly interface with the PyTorch ecosystem and its optimization algorithms. We design and validate a complete forward–inverse modeling workflow that leverages surface velocity and topography data as observational constraints to invert for nonlinear mantle rheology parameters across a suite of synthetic scenarios with varying complexity.

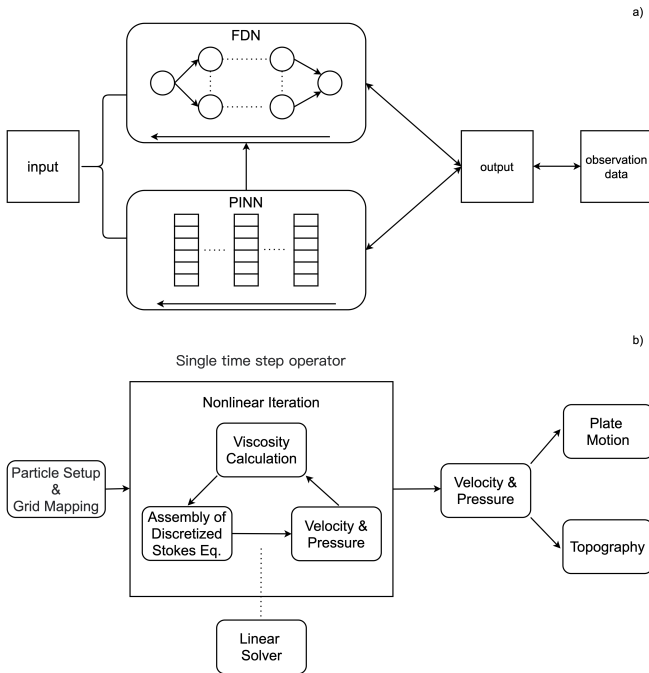


Figure 1. The overall framework of AD. (a) Comparison of frameworks of PINNs with the finite difference network. (b) Detailed implementation of the finite difference network that solves the Stokes equations.

## 2 METHOD

AD is based on the concept of a computational graph, which represents a sequence of operations as a directed graph where nodes correspond to variables and edges represent dependencies and operations. This graph-based approach is ubiquitous in modern deep learning frameworks, serving as the backbone for gradient-based optimization in neural networks. The overall framework of this study is analogous to the classical Physics-Informed Neural Networks (PINNs), except that the neural network structure in the PINNs is replaced by a finite difference network (FDN) that solves the Stokes equations numerically. In the traditional PINNs framework, the input consists of a set of model parameters of interest, such as temperature and viscosity. These parameters are processed through the neural network structure in PINNs to perform forward simulations, generating predicted values of the target physical fields, such as velocity and stress fields. Subsequently, these predicted values are compared with observational data and/or physical equation constraints to compute the errors and construct the loss function (Fig.1a). Unlike traditional neural networks, FDN implements the numerical solution of partial differential equations through a combination of multiple simple nodes and custom-extended complex nodes. The construction of FDN requires translation of finite difference computational steps into computational nodes, which are then interconnected and organized through a computational graph framework to form a complete forward modeling workflow. The primary nodes of FDN include interpolation operators, discretized linear system assembly for the Stokes equations, viscosity computation and linear solvers (Fig.1b).

To optimize the input parameters, PINNs utilizes automatic differentiation that computes gradient backpropagation based on computational graphs. This process propagates gradient information from the output backward to the input layer, followed by parameter updates using gradient-based optimizers. Similarly, automatic differentiation is implemented within the finite difference networks (FDN) to compute the gradient. The computational graph is automatically generated based on the numerical operators of the FDN, ensuring both the accuracy and efficiency of the forward and backward propagation processes.

### 2.1 Geodynamic forward modeling

#### 2.1.1 Governing equations

On geological time scales, the properties of mantle rocks are generally considered analogous to those of highly viscous fluids. Under such conditions, the deformation of these high-viscosity fluids can be accurately described by the Stokes equations, with the inertial terms neglected (Blackwell et al., 1990; Christensen & Yuen, 1985). We also approximate the Earth's mantle as an incompressible fluid under the Boussinesq approximation, where the density variation takes effect only for the buoyancy term in the momentum equation (Christensen & Yuen, 1985). In two dimensions, the conservation of mass and momentum is written as:

$$\frac{\partial v_x}{\partial x} + \frac{\partial v_y}{\partial y} = 0 \quad (1)$$

$$\frac{\partial \sigma_{xx}}{\partial x} + \frac{\partial \sigma_{xy}}{\partial y} - \frac{\partial p}{\partial x} + \rho \cdot g_x = 0 \quad (2)$$

$$\frac{\partial \sigma_{yy}}{\partial y} + \frac{\partial \sigma_{xy}}{\partial x} - \frac{\partial p}{\partial y} + \rho \cdot g_y = 0 \quad (3)$$

where  $v_x$  and  $v_y$  represent the  $x$  and  $y$  components of the velocity vector  $\vec{v}$ ,  $\sigma_{xx}$ ,  $\sigma_{xy}$  and  $\sigma_{yy}$  denote the deviatoric stress components,  $p$  represents the pressure,  $\rho$  is the density, and  $\vec{g} = (g_x, g_y)$  corresponds to the gravitational acceleration.

Density is generally considered a function of temperature and composition, and its variation can be described by the following equation:

$$\rho = \rho_c \cdot (1 - \alpha \cdot (T - T_0)), \quad (4)$$

where  $\rho_c$  and  $T_0$  represent the reference density for a specific composition  $c$  and the reference temperature, respectively;  $T$  is the current temperature;  $\alpha$  is the thermal expansion coefficient, taken here as  $3 \cdot 10^{-5}$ . Here,  $T_0$  is set to room temperature, with a value of 273 K.

In viscous fluid models, the constitutive relation between stress and strain rate can be defined as:

$$\sigma_{xx} = 2\eta\epsilon_{xx}, \quad \sigma_{yy} = 2\eta\epsilon_{yy}, \quad \sigma_{xy} = 2\eta\epsilon_{xy} \quad (5)$$

where  $\eta$  represents the viscosity, and  $\epsilon_{xx}$ ,  $\epsilon_{yy}$  and  $\epsilon_{xy}$  denote the strain rate components.

#### 2.1.2 Finite difference formulation of the governing equations

In the fully staggered grid configuration shown in Figure 2, the finite difference scheme for the Stokes equations as ex-

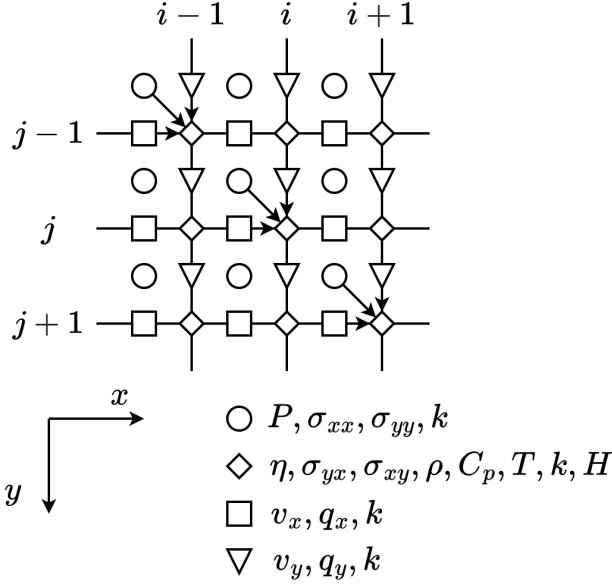


Figure 2. The fully staggered grid configuration, where Pressure ( $P$ ) and normal stress ( $\sigma$ ) are defined at the cell centers, while velocity components ( $v_x, v_y$ ) are defined at the cell edges, and temperature ( $T$ ), shear stress ( $\sigma_{xy}, \sigma_{yx}$ ) and viscosity ( $\eta$ ) are defined at the cell vertices. This grid design effectively enhances the stability and accuracy of solutions in numerical simulations.

pressed in the following discretized form, is suitable for geodynamic simulations of high-viscosity fluids (Gerya, 2019).

For any grid point  $(i, j)$ , the momentum conservation equations can be discretized in the  $x$ -direction and  $y$ -direction as shown in equations (6) and (7), respectively. The momentum conservation equation consists of three components: the numerical difference of the normal stress, the shear stress, and the pressure:

$$\frac{\sigma_{i+1,j}^{xx} - \sigma_{i,j}^{xx}}{x_{i+1,j} - x_{i,j}} + \frac{\sigma_{i,j}^{xy} - \sigma_{i,j-1}^{xy}}{y_{i,j} - y_{i,j-1}} - \frac{P_{i+1,j} - P_{i,j}}{x_{i+1,j} - x_{i,j}} = -\frac{\rho_{i,j} + \rho_{i,j-1}}{2} g_x, \quad (6)$$

$$\frac{\sigma_{i,j+1}^{yy} - \sigma_{i,j}^{yy}}{y_{i,j+1} - y_{i,j}} + \frac{\sigma_{i,j}^{xy} - \sigma_{i-1,j}^{xy}}{x_{i,j} - x_{i-1,j}} - \frac{P_{i,j+1} - P_{i,j}}{y_{i,j+1} - y_{i,j}} = -\frac{\rho_{i,j} + \rho_{i-1,j}}{2} g_y \quad (7)$$

The stress terms  $\sigma_{xx}$ ,  $\sigma_{yy}$ , and  $\sigma_{xy}$  in equations (6) and (7) need to be further discretized as follows:

$$\sigma_{i,j}^{xx} = 2\eta_{i,j} \frac{v_{i,j}^x - v_{i-1,j}^x}{x_{i,j} - x_{i-1,j}}, \quad (8)$$

$$\sigma_{i,j}^{yy} = 2\eta_{i,j} \frac{v_{i,j+1}^y - v_{i,j}^y}{y_{i,j+1} - y_{i,j}}, \quad (9)$$

$$\sigma_{i,j}^{xy} = \eta_{i,j} \left( \frac{v_{i,j+1}^x - v_{i,j}^x}{y_{i,j+1} - y_{i,j}} + \frac{v_{i+1,j}^y - v_{i,j}^y}{x_{i+1,j} - x_{i,j}} \right), \quad (10)$$

This way, each term in equations (6) and (7) is discretized in the form of velocity or pressure differences. The

discretization of the stress terms (equations (8), (10), and (9)) further links the velocity gradients to viscosity, ensuring that the viscosity values at grid points can be used to construct the complete linear matrix for the momentum equations.

For an incompressible fluid, the discretized form of the mass conservation equation can be expressed as:

$$\frac{v_{i+1,j}^x - v_{i,j}^x}{x_{i+1,j} - x_{i,j}} + \frac{v_{i,j+1}^y - v_{i,j}^y}{y_{i,j+1} - y_{i,j}} = 0, \quad (11)$$

The discretized momentum conservation equations (Equations (6) and (7)) and the mass conservation equation (Equation (11)), together form the linear system that is solved using direct matrix inversion for velocity and pressure.

### 2.1.3 Rheology

The effective viscosity ( $\eta_{\text{eff}}$ ) is a critical parameter that characterizes the rheological behavior of materials under various mechanical and thermodynamic conditions. For simplicity and to focus on the deformation characteristics of subducting slabs, this study considers only dislocation creep and plastic deformation. These two mechanisms describe the deformation properties of materials under low-temperature and high-stress conditions and can effectively capture the rheological behavior of subducting slabs (Hu et al., 2024).

Under the dislocation creep mechanism, the viscosity of the material is controlled by

$$\eta_{\text{dis}} = A_{\text{disl}}^{1/n} \cdot \dot{\epsilon}_{ii}^{(1/n-1)} \cdot \exp\left(\frac{E}{nRT}\right) \quad (12)$$

The physical meanings of the symbols are as follows:  $\eta_{\text{dis}}$  represents the viscosity under dislocation creep;  $\dot{\epsilon}_{ii}$  is the second invariant of the strain rate tensor, reflecting the material's flow rate;  $A_{\text{disl}}$  is the pre-exponential factor related to the material properties;  $E$  is the activation energy;  $n$  is the stress exponent, which determines the nonlinear response of the material to strain rate;  $R$  is the gas constant, with a value of  $8.314 \text{ J} \cdot \text{mol}^{-1} \cdot \text{K}^{-1}$ ; and  $T$  is the absolute temperature.

Plastic deformation is primarily governed by the yield strength of the material, which is prescribed as a constant  $\sigma$  value of 200 MPa in this study. For simplicity, we assume  $\mu = 0$  and a constant yield stress for the whole domain. Under conditions of plastic deformation, the viscosity  $\eta_{\text{plas}}$  is expressed as:

$$\eta_{\text{plas}} = \frac{\sigma}{2\dot{\epsilon}_{ii}} \quad (13)$$

To account for both dislocation creep and plastic deformation, the effective viscosity ( $\eta_{\text{eff}}$ ) is defined as the harmonic mean of the two mechanisms:

$$\frac{1}{\eta_{\text{eff}}} = \frac{1}{\eta_{\text{plas}}} + \frac{1}{\eta_{\text{dis}}} \quad (14)$$

Since the viscosity is nonlinear, we solve for velocity and pressure iteratively using the fixed point iteration until convergence is reached.

## 2.2 Automatic differentiation and backward modeling

The mathematical foundation of AD lies in the chain rule. Its core concept is to decompose a complex function into a series of basic operations (such as addition, multiplication, and exponential functions) and to record the dependencies of these operations by constructing a computational graph. The computational graph is a Directed Acyclic Graph (DAG) (Rall, 1981), where each node represents a variable and the edges represent dependencies and computational operations. Automatic Differentiation (AD) operates primarily in two modes: forward mode and reverse mode. Forward mode propagates derivatives from inputs to outputs, requiring one pass through the computational graph for each input variable. This becomes inefficient for functions with many inputs, as the computational cost scales linearly with the number of input parameters. Reverse mode, conversely, first evaluates the function and then propagates derivatives backward from outputs to inputs. For functions with many inputs but few outputs as in our case in geophysical inversion where we have many rheological parameters but a single scalar loss function, reverse mode calculates all partial derivatives in just one backward pass. This study adopts the reverse mode for gradient computation.

In the gradient computation phase, we employ reverse-mode automatic differentiation (AD) to efficiently obtain the sensitivities of the loss function with respect to model parameters. The overall computational workflow is first decomposed into a series of operators, each representing a discrete numerical operation, and a corresponding computational graph is constructed. This graph systematically records the dependency relationships between inputs and outputs across the entire forward model, enabling reverse traversal during the backpropagation stage. By propagating gradients backward through the graph, we can precisely evaluate the derivatives of the loss function with respect to each inversion parameter. Once the gradients are obtained, we utilize a gradient-based local optimization algorithm, L-BFGS (Limited-memory Broyden–Fletcher–Goldfarb–Shanno) (Liu & Nocedal, 1989), to iteratively update the model parameters. L-BFGS offers an efficient trade-off between memory usage and optimization performance by approximating second-order information without explicitly computing the full Hessian. Its robustness and rapid convergence make it particularly well-suited for inverse modeling in geodynamics. Through repeated iterations of this AD-based gradient evaluation and L-BFGS optimization, we achieve accurate recovery of the target rheological parameters.

## 3 SYNTHETIC DATA INVERSION

To evaluate the applicability and effectiveness of the proposed method for inverting complex nonlinear rheological parameters, we designed a series of numerical experiments. Two representative geometric configurations were constructed: one featuring a single subduction zone and the other incorporating three subduction zones, to simulate plate subduction processes under different tectonic regimes. For each model, synthetic surface velocity and dynamic topography data were generated through forward simulations, where the dynamic topography was computed from the surface normal stress. These synthetic datasets were treated

as proxies for "true" observations and used to assess the inversion performance. The observational data were categorized into two scenarios: idealized and more realistic. In the ideal case, the data were noise-free and fully resolved. For the more realistic scenario, several observational constraints were introduced. Specifically, to mimic the absence of GPS coverage over oceanic plates, we assumed that each plate behaves as a rigid body, and its motion is represented by a constant average velocity. In addition, random noise was added to the synthetic observations to simulate measurement uncertainties. In all inversion experiments, the geometry and thermal structure of the model were assumed to be known. The Stokes equations were solved numerically to obtain the velocity and surface stress fields. Gradients of the loss function with respect to model parameters were computed efficiently and accurately using AD. These gradients were then used to iteratively update the model parameters via gradient-based optimization, allowing for the robust recovery of key rheological properties in the mantle and weak shear zones.

### 3.1 The reference three-subduction model: forward and inverse

The reference model (Model 1) spans approximately 4500 km horizontally and extends to a depth of 800 km, as illustrated in Fig. 3. The computational domain is discretized using a structured mesh with  $675 \times 85$  grid points, the mesh is refined in the vicinity of subduction-related weak zones, where the resolution increases to 3 km, enabling better representation of localized deformation and strain localization. The model domain comprises multiple geological units, each assigned distinct structural or rheological properties, including the lithospheric mantle, weak shear zones, subducting slabs, upper mantle, and lower mantle. The setup incorporates three subduction zones with varying slab geometries and multiple interacting plates of different lengths. The first subduction zone is located at approximately 900 km along the horizontal axis, with a steep slab dipping at about  $45^\circ$  and extending down to 350 km depth. The second subduction zone lies near 2400 km, featuring a shallower dip angle of approximately  $30^\circ$  and a slab descending to 250 km. This zone includes a spreading center to its left, mimicking the effects of back-arc extension driven by trench retreat. At 3400 km, a broader slab extends to 660 km depth, flattening near the base of the transition zone. In contrast to the other slabs, its motion is significantly influenced by the resistance from the high-viscosity lower mantle.

Although the lithosphere and upper mantle are distinct geological units, they share the same viscosity parameters. The only difference lies in their temperature structures. The temperature field of the model is generated using a half-space cooling model, with the plates and slabs assumed to have an age of 60 Myr. The reference density for all units is  $\rho_c = 3300 \text{ kg/m}^3$ . The motions of plates are driven by the negative buoyancy of the cold slabs. The viscosity of the weak shear zones along plate interface at subduction zones and the viscosity of the lower mantle are set as constant values, with the weak zone assigned a viscosity of  $10^{19} \text{ Pa} \cdot \text{s}$  and the lower mantle assigned a viscosity of  $10^{23} \text{ Pa} \cdot \text{s}$ , while the viscosities of other geological units are calculated using the rheological formulas (12), (13), and (14). For the lithosphere

Table 1. Inverse models under different geometric and observational configurations. The table lists the final inverted parameter values, including the pre-exponential factor for dislocation creep  $A_{\text{disl}}$ , activation energy  $E_{\text{disl}}$ , stress exponent  $n$ , constant viscosity of the weak zone  $A_c$ , and yield stress  $\sigma$ . The relative errors between the prediction and observation for both the surface velocity and topography (columns “Vel. Error” and “Topo. Error”), along with the relative errors for noisy data (columns “Noisy Vel. Err.” and “Noisy Topo. Err.”), are reported. Relative error is computed according to Equation (20).

Model	Geometry	Observations	Iter. Num.	$A_{\text{disl}}$ Pa <sup>n</sup> · s	$E_{\text{disl}}$ kJ/mol	$n$ (-)	$A_c$ Pa · s	$\sigma$ MPa	Vel. Error	Topo. Error	Noisy Vel. Err.	Noisy Topo. Err.
Model 1	Three-slab	Surface velocity and topography	43	$10^{16.00}$	534.0	3.50	$10^{19.00}$	200.0	3.68E-6	2.09E-6	/	/
Model 2	Three-slab	Plate motion and topography	31	$10^{16.00}$	534.0	3.50	$10^{19.00}$	200.0	2.14E-6	2.28E-6	/	/
Model 3	Three-slab	Noisy plate motion and topography	49	$10^{17.43}$	488.9	3.47	$10^{19.01}$	199.2	6.58%	4.23%	9.33%	6.60%
Model 4	Three-slab	Plate motion only	76	$10^{16.00}$	534.0	3.50	$10^{19.00}$	200.0	2.13E-6	2.28E-6	/	/
Model 5	Three-slab	Noisy plate motion	59	$10^{19.14}$	460.0	3.54	$10^{19.44}$	140.8	16.30%	15.41%	9.38%	/
Model 6	Three-slab	Surface topography only	33	$10^{16.00}$	534.0	3.50	$10^{19.00}$	200.0	1.98E-5	1.98E-6	/	/
Model 7	Three-slab	Noisy surface topography	38	$10^{16.04}$	534.6	3.51	$10^{19.02}$	199.5	3.73%	0.31%	/	4.11%
Model 8	Single-slab	Surface velocity and topography	54	$10^{16.00}$	534.0	3.50	$10^{19.00}$	200.0	1.58E-6	1.72E-6	/	/
Model 9	Single-slab	Surface velocity only	66	$10^{4.12}$	827.2	3.33	$10^{19.18}$	234.7	0.48%	30.73%	/	/

and upper mantle, the viscosity of dislocation creep is characterized by a pre-exponential factor  $A_{\text{disl}} = 10^{16} \text{ Pa}^{-n} \text{ s}$ , an activation energy  $E = 534 \text{ kJ/mol}$ , a stress exponent  $n = 3.5$ , and a yield stress  $\sigma = 200 \text{ MPa}$ . The final effective viscosity is confined within the range of  $10^{18} \text{ Pa} \cdot \text{s}$  to  $10^{25} \text{ Pa} \cdot \text{s}$ . From model results, the minimum viscosity with a value of  $10^{19} \text{ Pa} \cdot \text{s}$  is observed in the weak shear zones, while the maximum viscosity of  $10^{25} \text{ Pa} \cdot \text{s}$  occurs within the plate interior. The viscosity structure (Fig.3c) regulates the deformation of each geological unit and the observational data at the surface which in turn can be used to constrain rheological parameters.

We construct a forward model using the aforementioned rheological parameters to generate synthetic surface velocity and topography data, which serve as observational constraints for the inverse model. We first conduct parameter inversion in an idealized, noise-free configuration, allowing for a more direct evaluation of inversion accuracy and the convergence behavior. The parameters to be inverted in this study include the pre-exponential factor  $A_{\text{disl}}$ , the strain rate exponent  $n$ , the activation energy  $E_{\text{disl}}$ , the yield stress  $\sigma$ , and the weak zone viscosity  $\eta(A_c)$ .

The loss function ( $\mathcal{L}$ ) is defined using both surface velocities and topography. It is worth noting that topography  $h$  is converted from the normal stress  $\sigma_{yy}$  at the surface using the following relationship:  $h = \frac{\sigma_{yy}}{\Delta\rho \cdot g_0}$ , where  $\Delta\rho$  denotes the density contrast between seawater and the mantle, and  $g_0$  is the gravitational acceleration constant. To account for differences in physical scales, we first normalize the observed and predicted velocity and topography data using the mean and standard deviation of the observed data. This enhances numerical robustness and facilitates efficient parameter estimation. Taking the velocity component  $v_x$  as an example, the normalization process is defined as:

$$\mu_{v_x} = E(v_x^{\text{obs}}), \quad \sigma_{v_x} = \text{std}(v_x^{\text{obs}}), \quad (15)$$

$$\tilde{v}_x^{\text{pred}} = \frac{v_x^{\text{pred}} - \mu_{v_x}}{\sigma_{v_x}}, \quad \tilde{v}_x^{\text{obs}} = \frac{v_x^{\text{obs}} - \mu_{v_x}}{\sigma_{v_x}}, \quad (16)$$

where  $\mu_{v_x}$  and  $\sigma_{v_x}$  represent the mean and standard

deviation of the observed velocity. A similar standardization process is applied to the surface topography  $h$ :

$$\mu_h = E(h^{\text{obs}}), \quad \sigma_h = \text{std}(h^{\text{obs}}), \quad (17)$$

$$\tilde{h}^{\text{pred}} = \frac{h^{\text{pred}} - \mu_h}{\sigma_h}, \quad \tilde{h}^{\text{obs}} = \frac{h^{\text{obs}} - \mu_h}{\sigma_h}. \quad (18)$$

Using the normalized data, the total loss functions for velocity and topography are defined as:

$$\mathcal{L} = \frac{1}{M} \sum_{i=1}^M (\tilde{v}_{x,i}^{\text{pred}} - \tilde{v}_{x,i}^{\text{obs}})^2 + \frac{1}{N} \sum_{i=1}^N (\tilde{h}_i^{\text{pred}} - \tilde{h}_i^{\text{obs}})^2, \quad (19)$$

where  $M, N$  denotes the total number of observations for velocities and topography, respectively.

To ensure the stability and efficiency of the inversion process, we define the following convergence criteria. First, the optimization automatically terminates when the maximum number of iterations is reached ( $\text{max\_iter} = 200$ ), in order to prevent excessive computational cost due to infinite loops. Second, if the  $\ell_2$ -norm of the gradient of the loss function with respect to the model parameters  $\theta$  satisfies  $\|\nabla\mathcal{L}(\theta)\|_2 < 10^{-9}$ , the iteration is deemed to have approached an optimal solution and will stop. Third, if the  $\ell_2$ -norm of the parameter update between two consecutive steps is less than  $10^{-10}$ , i.e.,  $\|\theta_{k+1} - \theta_k\|_2 < 10^{-10}$ , the parameters are considered to have converged. Additionally, in noise-free (clean) observational settings, the inversion is regarded as successfully converged when the total loss  $\mathcal{L}$  falls below  $10^{-8}$ , indicating that the model has achieved sufficient accuracy.

Selecting appropriate initial parameter values significantly impacts inversion performance, which constitutes a form of “hyperparameter tuning”. However, due to the inherent complexity of the objective function, manually identifying the optimal starting points remains challenging. Consequently, initial parameters are treated as hyperparameters, and Bayesian optimization, a widely adopted hyperparameter tuning approach in machine learning (Snoek et al., 2012),

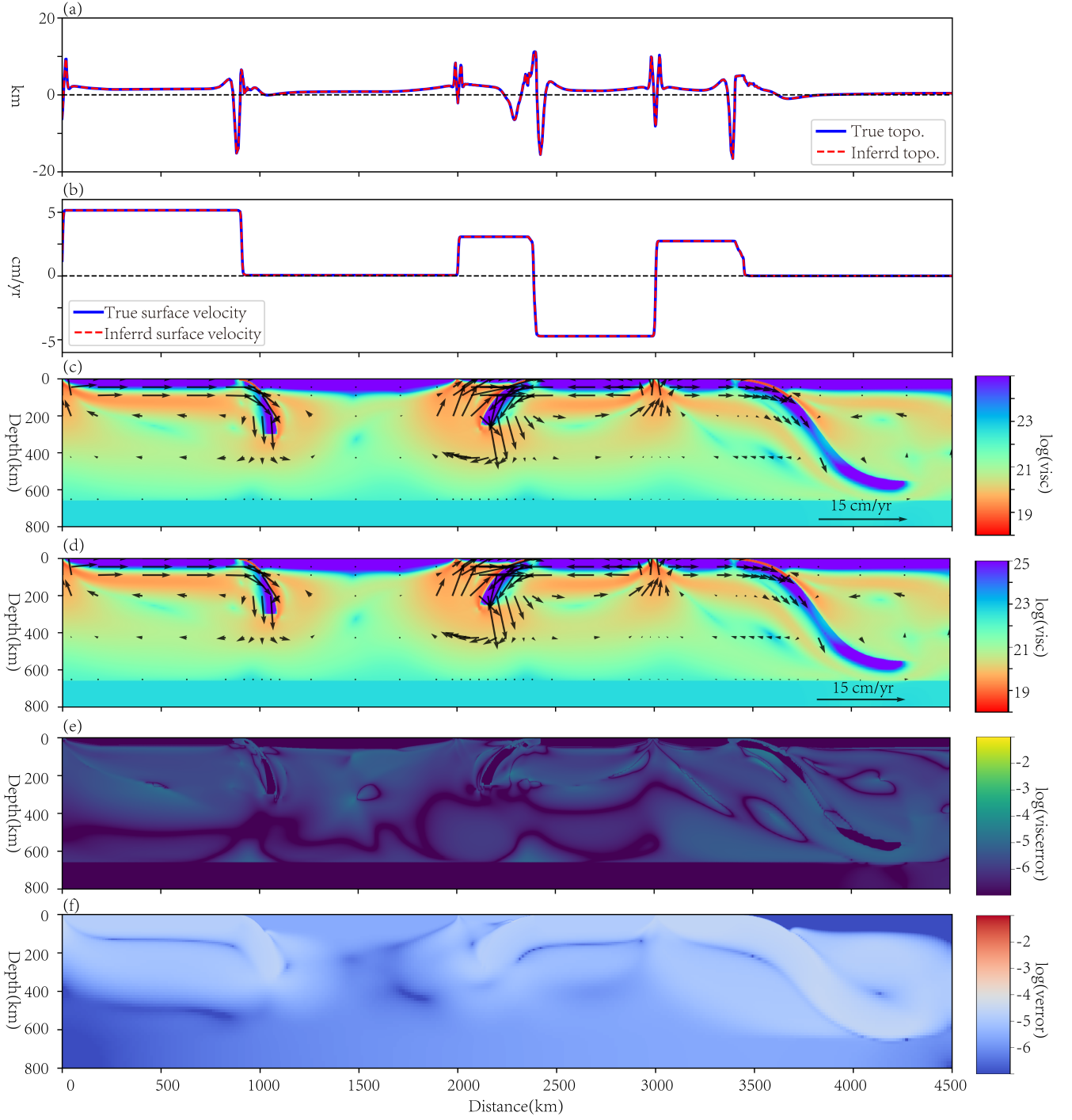


Figure 3. The reference three-subduction model (Model 1), showing both the recovered topography, velocity and viscosity structures and the synthetic observational structures. (a) The fit between the observed topography and the inferred topography. (b) The fit between the observed surface velocity and the inferred surface velocity. (c) The synthetic viscosity and velocity fields using the true parameters. (d) The recovered viscosity and velocity fields using the inverted parameters. (e) The viscosity error between the synthetic data and the inversion. (f) The velocity error between the synthetic data and the inversion.

is utilized to systematically search for optimal initial values. So we apply Bayesian optimization to select suitable starting parameters for key rheological and training hyperparameters. The optimization is conducted over a continuous parameter space, defined as follows:  $\log_{10} A_{\text{disl}}^{\text{init}} \in [12.5, 13.5]$ ,  $E_{\text{disl}}^{\text{init}} \in [250, 350]$ ,  $n^{\text{init}} \in [1, 2]$ ,  $\log_{10} A_c^{\text{init}} \in [20, 21]$ , yield

$\text{stress}^{\text{init}} \in [50, 100]$ . Note that usually these intervals reflect physically reasonable ranges and practical prior knowledge for dislocation creep, composite rheology, and optimizer stability. But in this case, we deliberately select the ranges that deviate away from the true values to test the robustness of the inversion method. The core principle of Bayesian

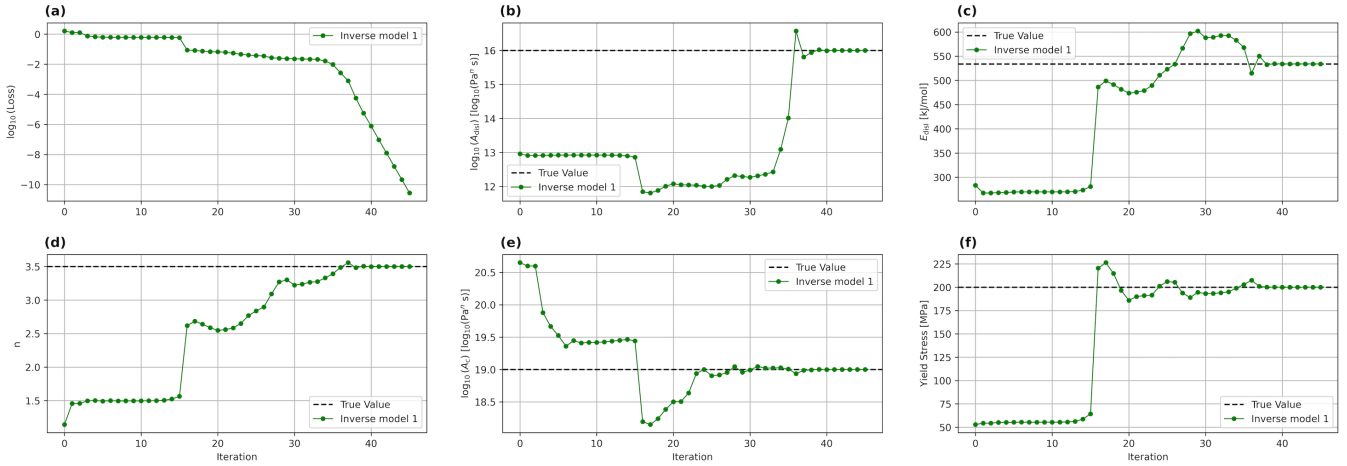


Figure 4. The reference three-subduction model (Model 1), showing the evolution of the loss function (a) and the five inverted rheological parameters (b–f) over the course of iterations. Green circles connected by lines represent the inverted parameter values, while the dashed lines indicate the corresponding true values.

optimization lies in leveraging probabilistic modeling and intelligent sampling to perform a global search for the optimum of an objective function. Typically, a Gaussian Process (GP) is used to model the objective function, and acquisition functions—such as Expected Improvement (EI), Upper Confidence Bound (UCB), or Probability of Improvement (PI)—guide the selection of the next sampling point. In this study, we adopt the Probability of Improvement (PI) strategy as the acquisition function. This method balances exploration and exploitation by evaluating the likelihood that a new sampling point will improve upon the current best value. Each iteration of Bayesian optimization updates the Gaussian Process model based on newly acquired information, progressively refining the search for optimal initial parameters (Snoek et al., 2012). In our inversion framework, each set of initial values undergo five independent inversion runs. The best-performing result among the five is selected for presentation. The optimal solution is chosen based on the following criteria: if the inversion successfully converges and the total loss is less than  $10^{-8}$ , the solution with the fewest iterations is selected; if the inversion does not achieve a sufficiently small loss, the solution with the lowest loss function value is taken as the representative result.

The evolution of the five inverted parameters during the inversion process and the final converged results are illustrated in Fig. 4. The initial loss function exhibits a relatively high value, which rapidly decreases to the order of  $10^{-11}$  after approximately 40 iterations, indicating an exceptionally high level of accuracy in fitting the observational data. Examining the iteration trends of individual parameters, the pre-exponential factor for dislocation creep,  $\log_{10}(A_{\text{disl}})$ , starts at approximately 13.0 with minimal early-stage variation but experiences a sharp increase to 16 after 37 iterations. The activation energy for dislocation creep,  $E_{\text{disl}}$ , begins at 280 kJ/mol, and ultimately stabilizes at 534 kJ/mol after 37 iterations. The stress exponent  $n$  starts from 1.2, gradually increases from iterations 12, and eventually converges to 3.5 at iterations 37. The viscosity parameter for the weak zone,  $\log_{10}(A_c)$ , initially exceeds the true value but decreases rapidly during early iterations, stabilizing at 19 after 30 iterations. The yield stress  $\sigma$ , which starts at a value sig-

nificantly lower than the true value, increases rapidly after 10 iterations and finally stabilizes at 200 MPa. Despite some degree of oscillation in these parameters throughout the optimization process, the final converged values deviate from the true values by no more than  $10^{-5}$ , demonstrating the robustness and accuracy of the proposed inversion method under ideal noise-free conditions. To further evaluate the accuracy of the inferred velocity and viscosity fields, we compared the inferred results using the recovered parameters with the observational data using the true parameters. As shown in Fig. 3a,b, the inferred surface topography and velocity align almost perfectly with the observations. The comparison of the viscosity and velocity fields (Fig. 3c,d) further confirms that the inferred fields using the recovered parameters exhibit minimal discrepancies from the observational data.

To systematically evaluate the discrepancies between the inferred and the observed data, we further perform a quantitative analysis of the errors. The relative error is defined as follows:

$$\text{Relative Error} = \frac{\sum |\hat{x}_{\text{pred}} - x_{\text{obs}}|}{\sum |x_{\text{obs}}|}, \quad (20)$$

where  $\hat{x}_{\text{pred}}$  and  $x_{\text{obs}}$  denote the inferred and observed values, respectively. The viscosity field is plotted with respect to  $\log_{10}(\eta)$ . In the comparisons shown in Figure 3, the predicted dynamic topography in panel (a) almost perfectly overlaps with the observed values, with visually indistinguishable differences. The quantitatively evaluated relative error is merely  $2.09 \times 10^{-6}$ . Likewise, the inferred surface velocity shown in Figure 3(b) exhibits a relative error of only  $3.68 \times 10^{-6}$ , indicating that the reconstruction of both velocity and topography is highly accurate. A comparison between Figures 3(c) and (d) reveals that the overall structure of the reconstructed viscosity and velocity fields closely matches the true fields. On this basis, Figures 3(e) and (f) present the spatial distributions of the viscosity and velocity errors, respectively, across the entire domain. Here, the errors are visualized by the absolute differences between the predicted and observed values, where the values of viscosity are in logarithmic scale. The magnitude of the viscosity

errors is generally below  $10^{-5}$ , with slightly higher values observed in the shear zones surrounding the slabs. In contrast, the magnitude of the velocity errors is typically below  $10^{-4}$  cm/yr, with minor increases occurring within the slabs and the adjacent upper mantle regions. Overall, both fields suggest extremely low levels of misfit, confirming full convergence of the inversion. In summary, under noise-free conditions, the proposed method successfully recovers the rheological parameters with exceptional accuracy, while also reliably reproduces the surface topography and velocity data and the internal viscosity and velocity structures.

### 3.2 Effects of more realistic observational constraints - plate motion and data noise

While GPS measurements can provide accurate lateral motion for sites on lands, the motion of the oceanic plates can only be derived using magnetic lineations on the seafloor, which assumes rigid plates and provides a long-term averaged velocity for each plate within the span of each magnetic chron. This motion is called plate motion, which defines the motion of the rigid parts of a plate. To better approximate this observational condition, we adjust the setup of the observational data. Unlike Section 3.1, where all surface velocities are utilized, we only leverage the plate velocities in the interior of the plates about 50 km away from the plate boundaries (Fig. 5a). These velocities are assumed to be spatially uniform within each plate based on the rigid plate hypothesis. Based on this premise, we first conduct a parameter inversion experiment using ideal, noise-free plate motion and topography as observational inputs. The objective is to evaluate the accuracy and robustness of the proposed inversion method with less constraints from the motion of the surface nodes. Under noise-free conditions, we set the model as Model 2, which demonstrates excellent convergence and accuracy (Fig. 5). The inversion successfully converges within around 30 iterations, with the final loss function value reduced to below  $10^{-10}$ . The inverted parameters are nearly identical to the true values, with relative errors less than  $10^{-5}$ . For the recovered plate motion and topography, the relative fitting errors are both less than  $\sim 10^{-4}$ , indicating that the proposed method achieves extremely high-precision parameter reconstruction under noise-free conditions.

To further mimic uncertainties typically present in GPS measurements and paleomagnetically-constrained plate motion, we introduce artificial noise to the observational dataset using the following procedure. For plate motion, we apply a constant noise component  $\delta_v$  for each plate, drawn from a uniform distribution over the range  $[-0.5, 0.5]$  cm/yr. For surface topography, Gaussian noise  $\delta_h \sim \mathcal{N}(0, \sigma^2)$  is added, where the standard deviation  $\sigma$  is defined as 5% of the mean absolute value of the noise-free observations:

$$\sigma = \text{mean}(|h|) \times 0.05. \quad (21)$$

The noise-contaminated observational values are then computed as:

$$\tilde{v} = v + \delta_v, \quad \delta_v \sim \mathcal{U}(-0.5, 0.5), \quad (22)$$

$$\tilde{h} = h + \delta_h, \quad \delta_h \sim \mathcal{N}(0, \sigma^2), \quad (23)$$

where  $\tilde{v}$  and  $\tilde{h}$  represent the noisy plate motion and topography, respectively. Here,  $\delta_v$  and  $\delta_h$  denote the uniform and

Gaussian noise components added to the respective fields. This controlled noise addition strategy enables systematic evaluation of how various types of observational errors influence the inversion performance, providing both theoretical insight and methodological guidance for applying the inversion framework under real-world geophysical observation scenarios.

Model 3 represents the case where the observation of plate motion and topography is noisy. As shown by the parameter iteration results (Fig. 5), Model 3 requires more iterations to achieve convergence. Moreover, the presence of noise significantly affects certain parameters—particularly the pre-exponential factor for dislocation creep,  $A_{\text{disl}}$  (in units of  $\text{Pa}^n \cdot \text{s}$ ), and the activation energy  $E_{\text{disl}}$  (in units of kJ/mol). Specifically,  $A_{\text{disl}}$  is ultimately inverted to approximately  $10^{17.4} \text{Pa}^{-n} \cdot \text{s}$ , while  $E_{\text{disl}}$  converges to around 488.9 kJ/mol, both showing noticeable deviation from their truth values. In contrast, the stress exponent ( $n \approx 3.47$ ), weak shear zone viscosity ( $1.0 \times 10^{19.01} \text{Pa} \cdot \text{s}$ ), and yield strength (199.2 MPa) are less sensitive to noise, yielding results that remain closer to the true values, albeit slightly inferior to the noise-free scenario. Figures 5(a, b) present the fitting errors of plate motion and topography. When compared with the noise-free observational data, the relative error in plate velocity is only 6.58%, whereas it increases to 9.33% when compared with the noisy observations. Notably, the recovered observational field tends to align more closely with the noise-free data than with the noisy data. For topography, the relative error compared to the true value is 4.23%, while the error relative to noisy data is 6.60%. Overall, topography is less affected by observational noise and also displays a tendency to revert toward the true values during inversion. In summary, plate motion exhibits greater sensitivity to noise, resulting in noticeable deviations from the noisy observations in the final velocity field. Topography retains a relatively high fitting accuracy under joint observation conditions. Due to the Gaussian distribution of noise in topography, its statistical nature facilitates convergence toward the mean of the observational distribution, thereby mitigating the adverse effects of noise in the velocity data and improving reconstruction accuracy. On the parameter level,  $A_{\text{disl}}$  and  $E_{\text{disl}}$  are the most noise-sensitive parameters, with the largest deviations, further highlighting their susceptibility to observational uncertainty.

To further quantify the impact of different observation types on inversion accuracy, we evaluate two scenarios: using only plate motion data (Fig. 6) and using only topography data (Fig. 7). Under noise-free conditions, the inversion model using only clean plate motion observations (denoted as Model 4) successfully converges but requires significantly more iterations (approximately 87). This indicates that plate motion provides relatively weaker constraints on the model and exhibits an objective function where the minimum is more difficult to be reached. As shown in Fig. 6a, the value of the loss function  $\mathcal{L}$  decreases from an initial  $10^2$  to below  $10^{-10}$ , demonstrating that although the inversion process is slow, it eventually achieves high-accuracy convergence. Figures 6d–h show that the recovered parameters closely match the true values, with relative errors all below  $10^{-5}$ . The fitting results in Figs. 6a and 6b also confirm this, with relative errors between model outputs and observations below the  $10^{-4}$  threshold. When uniform noise

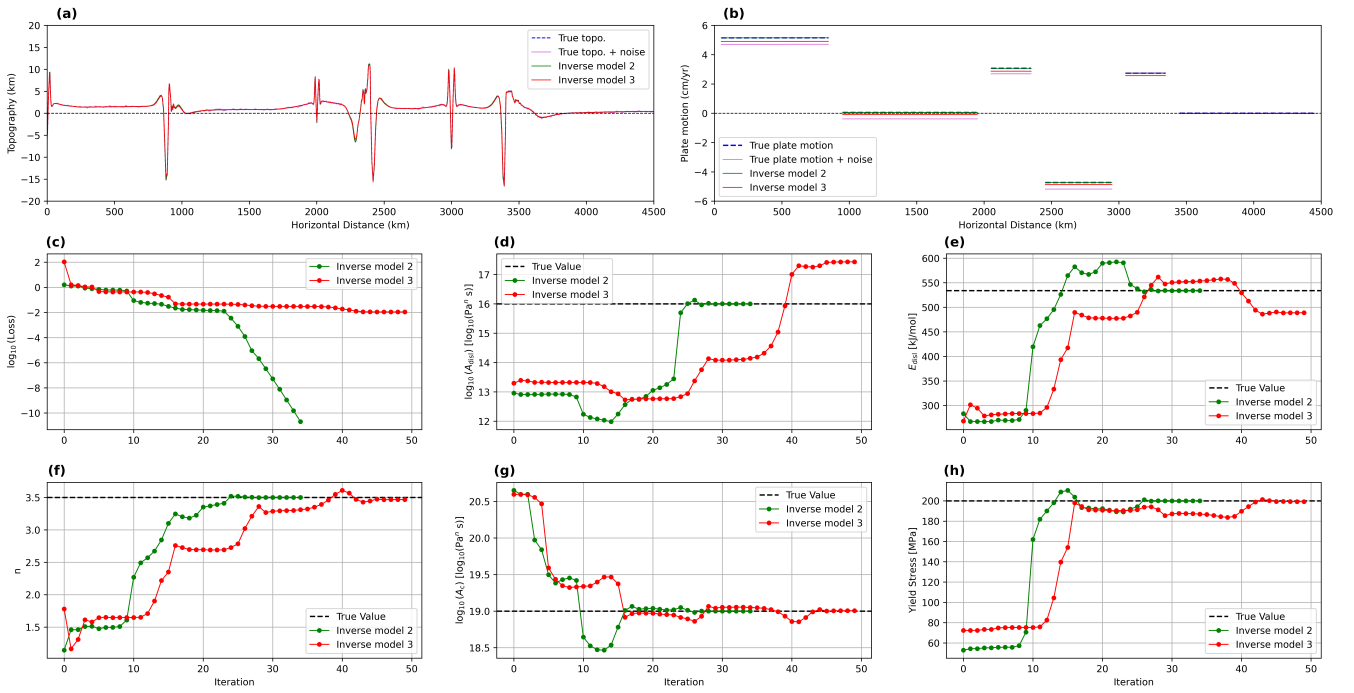


Figure 5. Parameter inversion results of Model 2 and Model 3, along with their fitting performance against observational data. Model 2 is based on Model 1 but uses noise-free plate motion and surface topography as observational inputs, while Model 3 builds upon Model 2 by introducing noise into both observational data. (a) The comparison between the observed surface topography and the inferred topography. (b) The comparison between the observed plate motion and the inferred plate motion. (c) The change of the loss function with the number of iterations. (d)-(h) The change of the five inverted parameters with the number of iterations.

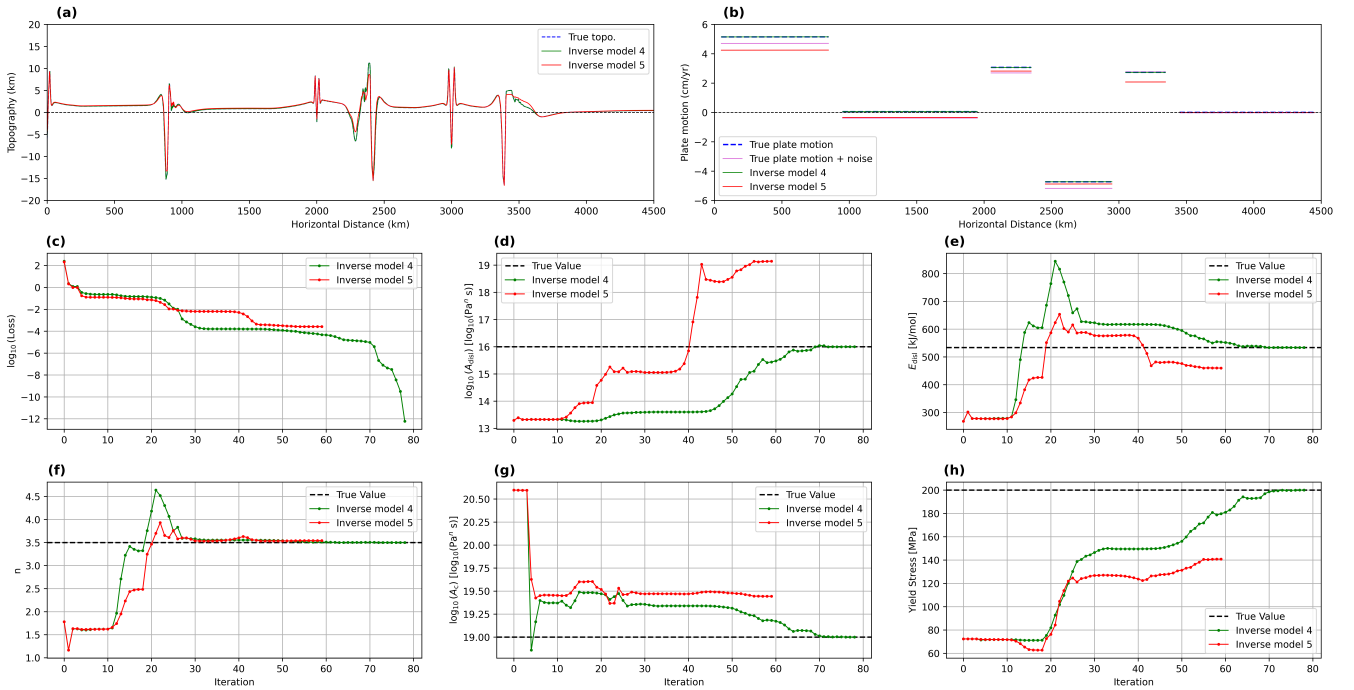


Figure 6. Parameter inversion results of Model 4 and Model 5, along with their fitting performance against observational data. Model 4 uses noise-free plate motion as the observational input, while Model 5 employs plate motion data with added noise. Other symbols are the same as Fig. 5.

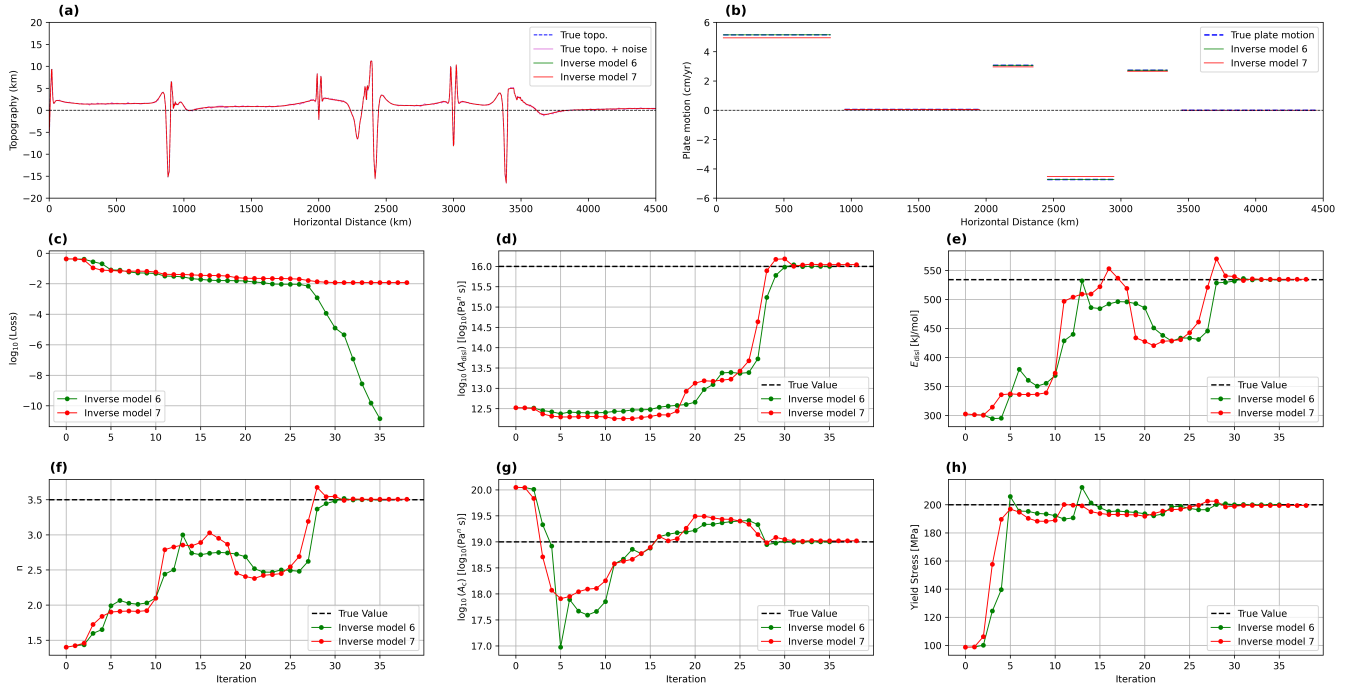


Figure 7. Parameter inversion results of Model 6 and Model 7, along with their fitting performance against observational data. Model 6 utilizes noise-free surface topography as the observational input, whereas Model 7 incorporates noise into the surface topography data. Other symbols are the same as Fig. 5.

is added to the plate velocity observations (Model 5), the inversion process is significantly hindered: the loss  $\mathcal{L}$  only decreases to about  $10^{-4}$  (Fig. 6c), and parameter deviations increase substantially (Figs. 6d–h). Specifically, while the stress exponent  $n$  converges to 3.54, close to the true value of 3.5, the remaining parameters exhibit notable deviations: the pre-exponential factor  $A_{\text{disl}}$  drifts to  $\sim 10^{19.14} \text{ Pa} \cdot \text{s}^{-n}$  (true value  $10^{16}$ ), the activation energy  $E_{\text{disl}}$  drops to about 460 kJ/mol (true value 534 kJ/mol), the weak shear zone viscosity increases to  $10^{19.44} \text{ Pa} \cdot \text{s}$  (true value  $10^{19}$ ), and the yield stress decreases to approximately 140 MPa (true value 200 MPa). Figures 6a and 6b show the fitting performance of Model 5: the relative error compared to the noise-free velocity field is 16.30%, while that relative to the noisy observations is about 9.38%. Because only noisy velocity data are used during inversion, the final solution aligns more closely with the noisy input rather than the noise-free values. In contrast, when surface stress is jointly observed under noisy conditions (as in the earlier joint-observation scenario), the velocity fitting error drops to 6.58%, indicating enhanced constraint capability. Moreover, topography—which is not included in Model 5’s observational data—shows substantial mismatch from the true values, with a relative error reaching 15.41%. Consistent with the conclusions drawn from Models 3 and 4, the inclusion of Gaussian-distributed topography noise helps regulate the inversion process and prevents overfitting to noisy plate motion. When topography constraints are removed, the model becomes significantly more sensitive to plate motion noise, leading to reduced inversion accuracy.

In contrast, using only topography as the observational input yields superior overall inversion performance. Under noise-free conditions (Model 6), the optimization converges rapidly within 33 iterations, with the final loss decreasing

to  $10^{-10}$  (Fig. 7a). The recovered parameters show excellent agreement with the true values (Fig. 7d–h), with all relative errors approaching 0. Additionally, the reconstructed plate motion and topography from Model 6 closely match the noise-free observation, with relative errors all approaching 0. Building on this, we introduced Gaussian-distributed observation noise to construct a more realistic scenario (Model 7), mimicking uncertainties in real-world geodetic data. Despite the added uncertainty, Model 7 maintains high inversion accuracy: all recovered parameters exhibit relative errors within approximately 0.1% (Fig. 7d–h). The recovered parameter values are  $\log_{10}(A_{\text{disl}}) = 16.04$ ,  $E_{\text{disl}} = 534.6 \text{ kJ/mol}$ ,  $n = 3.51$ ,  $\log_{10}(A_c) = 19.02$ , and  $\sigma = 199.5 \text{ MPa}$ . This performance is significantly better than those of Models 3 and 5 under similarly noisy conditions, indicating that surface topography data provide stronger constraints and greater robustness against noise in parameter inversion. Further comparison between the physical fields reconstructed by Model 7 and the observations reveals that the relative error in topography is 0.31% with respect to the true value and 4.11% relative to the noisy observations—slightly inferior to the noise-free Model 6 but still the best among all noisy-data models. Notably, even though plate velocity is not directly used as an input in Model 7, the relative error between the reconstructed and true velocity fields is only 3.73%, markedly lower than that in Models 3 and 5. This demonstrates that the physical information contained in surface topography observations indirectly enforces strong constraints on the plate velocity fields, substantially improving the overall inversion accuracy.

Under noise-free conditions, both single-type observations and the joint use of plate motion and surface topography yield high-accuracy inversion results. In the presence

of noise, the impact of imposing a constant shift to the motion of each plate on inversion performance is significantly greater than that of Gaussian noise in surface topography data. Due to the statistical properties of Gaussian noise in topography observations, the introduced perturbations are eventually smoothed out, which does not substantially influence the inversion robustness. Overall, in noisy scenarios, surface topography provides stronger constraints than plate motion, enhancing the accuracy and stability of the inversion process.

### 3.3 Effects of model complexity and Data Constraints

In the initial model design, we have employed a complex geometric structure incorporating three subduction zones to comprehensively simulate the dynamic processes resulting from multiple plate interactions. Subsequently, to evaluate the impact of geometric complexity on inversion convergence efficiency, we simplify the model to include only a single subduction zone (Model 8), thereby reducing the degree of geometric coupling within the system. By comparing single-subduction and multi-subduction configurations, we aim to elucidate the role of geometric complexity in influencing model convergence speed and accuracy, and provide valuable insights for parameter inversion in more intricate geological settings. In Model 8, we adopt the same viscosity formulation, rheological parameters, and temperature field as in Model 1, resulting in a similar distribution of viscosity and velocity fields (Fig. 8c), and used forward modeling to generate surface velocity and stress data as observations (Fig. 8a,b). This consistency is crucial in ensuring comparability between the two geometries, allowing us to directly assess the impact of structural complexity on inversion performance. The results indicate that despite the geometric simplification to a single-subduction configuration (Model 8), the inversion process still successfully converges (Fig. 8d-i), with the loss function reaching as low as  $10^{-10}$ , and the inferred rheological parameters closely matching the true values (Tab.1). However, compared to the three-subduction model, Model 8 requires additional iterations to achieve the same level of convergence, suggesting that geometric simplification reduces inversion efficiency to some extent.

Building upon this, we further change the strategy of observational constraints in Model 8 by retaining only the surface velocity data (Model 9). The results reveal a significant deterioration in inversion performance: none of the five sets of initial parameters selected via Bayesian optimization achieved convergence, and the loss function only reduced to approximately  $10^{-4}$ , contrasting sharply with the  $10^{-10}$  achieved in Model 8. Further analysis of the inverted parameters reveals that the weak zone viscosity and strain-rate exponent  $n$  are still well constrained: the recovered values are  $\log_{10}(A_c) = 19.18$  and  $n = 3.33$ , both exhibiting less than 5% deviation from the true values. In contrast, the error in the yield stress increases slightly, with an inverted value of 234.67 MPa, corresponding to a relative error of approximately 14.5%. The largest deviations are observed in the activation energy  $E_{\text{disl}}$  and the pre-exponential factor for dislocation creep  $\log_{10}(A_{\text{disl}})$ , which are recovered as 827.23 kJ/mol and 4.12, respectively—each showing errors exceeding 50% compared to their true values. These results suggest that under combined effects of geometric simplifi-

cation and limited observational data, certain rheological parameters—particularly the pre-exponential factor and activation energy—are prone to converge to inaccurate values, while the weak zone viscosity and  $n$  are comparatively easier to constrain, and the recoverability of yield stress lies between the two extremes. This reflects the distinct sensitivity of different parameters to surface velocities. Despite the deviation in parameter recovery, the velocity field restored using the inverted parameters from Model 9 still closely matches the observed field (Figure 8a), with good visual agreement and a relative error of only 0.48%. Although this is not as accurate as the convergence achieved under ideal noise-free conditions, it still reflects relatively strong inversion performance compared to other models with noise observations. In contrast, the restored topography (Figure 8b) exhibits a significantly larger error, with a relative discrepancy of approximately 30%. This indicates that when only the surface velocity generated from a single-subduction configuration is used for inversion, the velocity field can be accurately fitted, but the lack of sufficient constraints results in strong non-uniqueness and poor recovery of topography.

## 4 DISCUSSION AND CONCLUSION

This study integrates automatic differentiation with a finite-difference-based Stokes solver, enabling the simultaneous computation of forward models and automatic acquisition of the gradient of the loss function with respect to input parameters. We demonstrate an AD-enabled inversion framework implemented within the PyTorch environment for jointly recovering multiple nonlinear rheological parameters governing mantle flow. These parameters include the pre-exponential factor for dislocation creep  $A_{\text{disl}}$ , activation energy  $E_{\text{disl}}$ , stress exponent  $n$ , yield stress  $\sigma$ , and the constant viscosity  $A_c$  associated with the weak shear zone. Together, they comprise all the rheological control variables required for viscosity computation in the present model. In our implementation, the computational cost of AD-based inversion is approximately 1.5 to 2 times that of a single forward simulation, which is considered highly efficient in the context of geophysical inverse problems (Zhu et al., 2021; Coltice et al., 2023). However, the use of AD typically entails increased memory consumption, primarily due to the need to store intermediate variables during the reverse-mode backpropagation process. Leveraging the dynamic computational graph and flexible memory management capabilities of the PyTorch framework, future improvements may include memory-efficient strategies such as selective gradient tracking and global variable reuse. These enhancements can significantly reduce memory overhead, allowing AD to maintain high accuracy while achieving good scalability and computational efficiency.

In a simplified two-dimensional geodynamic configuration, numerical experiments demonstrate that the AD-based inversion framework exhibits excellent stability and high accuracy under varying levels of observational noise, data types, and geometric complexities. Under ideal noise-free conditions, the model achieves high-precision recovery of the target rheological parameters regardless of whether plate velocity or dynamic topography is used as the observational input. In terms of observational strategies, we adopted both

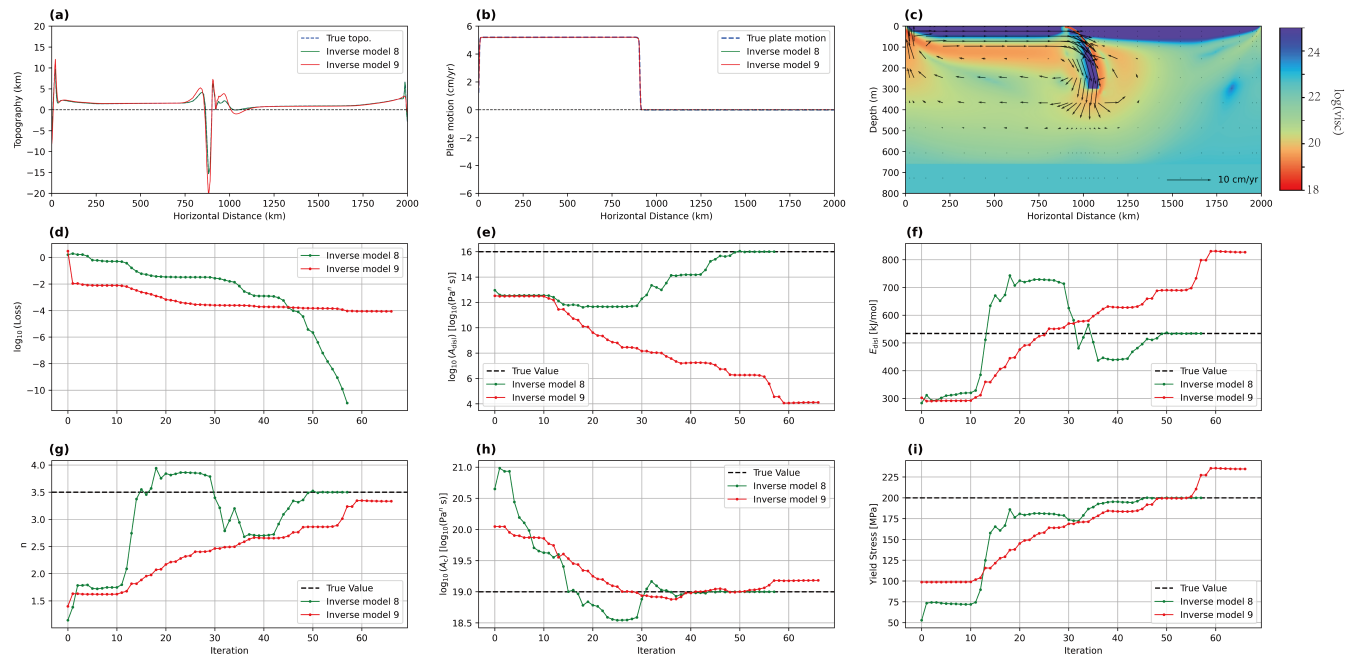


Figure 8. Inversion results of single-subduction models, where Model 8 uses both surface velocity and topography, while Model 9 employs surface velocity only, as observational constraints. (a) The comparison between the observed surface topography and the inferred topography. (b) The comparison between the observed surface velocity and the inferred surface velocity. (c) The true viscosity and velocity fields. (d) The change of the loss function with the number of iterations. (e)-(j) The change of the five inverted parameters with the number of iterations.

the “full surface velocity” scheme, similar to that used by Worthen et al. (2014), and the “average plate velocity” approach consistent with Ratnaswamy et al. (2015), in order to evaluate how different data acquisition strategies influence inversion performance. Furthermore, since mantle flow and viscosity structure directly control surface dynamic topography (Hager & Richards, 1989), and conversely, observed dynamic topography can provide constraints on the subsurface rheology, we incorporated surface topography as an additional observation type. This allows us to systematically compare its effectiveness in constraining nonlinear rheological parameters. Traditional adjoint-based approaches in geodynamics typically require elaborate mathematical derivations and the development of problem-specific adjoint solvers for each PDE or rheological model (Ratnaswamy et al., 2015; Hu et al., 2024), which significantly increases the complexity of implementation and maintenance. Meanwhile, parameter inversion using Markov Chain Monte Carlo (MCMC) methods is computationally expensive (Baumann et al., 2014b). In contrast, AD bypasses the need for explicit derivation of adjoint equations by automatically constructing computational graphs to evaluate gradients, thereby significantly simplifying development. Moreover, AD delivers gradients with near machine precision, avoiding discretization errors that often arise in manually implemented adjoint solvers.

One of the central objectives of this study is to verify whether it is feasible to jointly invert all major nonlinear viscosity parameters within a unified framework. Through a series of idealized numerical forward simulations, we confirm that, even under complex nonlinear viscosity laws, the AD-driven inversion algorithm is capable of accurately re-

covering five key parameters to near machine precision under noise-free conditions. Although the geometric and physical models are simplified, the successful inversion of parameters such as  $A_{\text{disl}}$  and  $\sigma$  demonstrates that the proposed method effectively captures the essential dynamics of subduction, lithosphere–mantle interaction, and weak shear zone behavior. Once observational noise is introduced, the inversion results exhibit clear sensitivity to the type of data used. Plate motion data with a constant shift as noise considering the rigid plate hypothesis, lead to slower convergence and larger deviations from the true parameter values. In contrast, surface topography data with Gaussian-distributed noise exhibit better numerical stability, allowing convergence toward the statistical mean while maintaining high inversion accuracy. Furthermore, surface topography generally provides stronger constraints than plate motion, particularly in high-noise scenarios where topography-based inversion delivers superior stability and fitting precision. Joint inversion using multiple observations usually improves the inversion performance (e.g. Models 3 versus 5). However, if the newly added data have low quality due to substantial errors or noise, the performance deteriorates (e.g. Models 3 versus 7). Geometric complexity also significantly affects inversion performance. Multi-slab models, due to their stronger mechanical coupling and localized dynamic features, enhance parameter recovery and accelerate convergence. In comparison, simplified single-slab models can still achieve successful inversion but typically require more iterations and exhibit increased sensitivity to data quality. In extreme cases, where only surface velocity observations are available, inversion accuracy deteriorates significantly, particularly for parameters

such as the pre-exponential factor for dislocation creep and activation energy.

Despite the demonstrated effectiveness and robustness of the automatic AD-based inversion framework in geodynamic problems, several promising directions remain for future exploration. Extending the current two-dimensional model to fully three-dimensional geodynamic simulations would substantially enhance the realism of Earth's internal structural representations, particularly when accounting for lateral variations in temperature and composition, as well as anisotropic viscosity. Future work could explore the integration of Physics-Informed Neural Networks (PINNs) to represent simplified forms of anisotropic rheology, an approach that has shown preliminary success in glacier dynamics modeling (Wang et al., 2025). Incorporating a broader range of geophysical observations—such as gravity anomalies, and intraplate stresses—will further strengthen model constraints, especially in data-sparse regions like the oceanic lithosphere. The framework developed here can be applied to regional studies using real observational datasets, and compared against viscosity models derived from geoid and seismological constraints (Steinberger & Calderwood, 2006), as well as inversion results obtained through adjoint-based methods (Hu et al., 2024). The current inversion framework is based on the assumption of steady-state Stokes flow, which limits its applicability to time-evolving processes. Future extensions may incorporate fully time-dependent models similar to those discussed by Coltice et al. (2023), enabling the method to capture dynamic geodynamic phenomena such as postseismic relaxation and slab rollback. Such developments would expand the utility of the AD-based inversion approach to a wider range of spatiotemporal geophysical processes.

## References

- Baumann, T. & Kaus, B. J., 2015. Geodynamic inversion to constrain the non-linear rheology of the lithosphere, *Geophysical Journal International*, 202(2), 1289–1316.
- Baumann, T. S., Kaus, B. J., & Popov, A. A., 2014a. Constraining effective rheology through parallel joint geodynamic inversion, *Tectonophysics*, 631, 197–211.
- Baumann, T. S., Kaus, B. J. P., & Popov, A. A., 2014b. Constraining effective rheology through parallel joint geodynamic inversion, *Tectonophysics*, 631, 197–211.
- Baydin, A. G., Pearlmutter, B. A., Radul, A. A., & Siskind, J. M., 2018. Automatic differentiation in machine learning: a survey, *Journal of machine learning research*, 18(153), 1–43.
- Becker, T. W. & Faccenna, C., 2011. Mantle conveyor beneath the tethyan collisional belt, *Earth and Planetary Science Letters*, 310(3-4), 453–461.
- Becker, T. W. & O'Connell, R. J., 2001. Predicting plate velocities with mantle circulation models, *Geochemistry, Geophysics, Geosystems*, 2(12).
- Behn, M. D., Hirth, G., & Elsenbeck, J. R., 2009. Implications of grain size evolution on the seismic structure of the oceanic upper mantle, *Earth and Planetary Science Letters*, 282(1), 178–189.
- Behr, W. M. & Becker, T. W., 2018. Sediment control on subduction plate speeds, *Earth and Planetary Science Letters*, 502, 166–173.
- Billen, M. I. & Hirth, G., 2007. Rheologic controls on slab dynamics, *Geochemistry, Geophysics, Geosystems*, 8(8).
- Blackwell, D. D., Steele, J. L., Frohme, M. K., Murphey, C. F., Priest, G. R., & Black, G. L., 1990. Heat flow in the Oregon cascade range and its correlation with regional gravity, Curie point depths, and geology, *Journal of Geophysical Research: Solid Earth*, 95(B12), 19475–19493.
- Buffett, B., 2006. Plate force due to bending at subduction zones, *J. Geophys. Res.*, 111.
- Buffett, B. A. & Rowley, D. B., 2006. Plate bending at subduction zones: Consequences for the direction of plate motions, *Earth and Planetary Science Letters*, 245(1), 359–364.
- Bunge, H.-P., Hagelberg, C., & Travis, B., 2003. Mantle circulation models with variational data assimilation: inferring past mantle flow and structure from plate motion histories and seismic tomography, *Geophysical Journal International*, 152(2), 280–301.
- Cai, S., Mao, Z., Wang, Z., Yin, M., & Karniadakis, G. E., 2021. Physics-informed neural networks (PINNs) for fluid mechanics: A review, *Acta Mechanica Sinica*, 37(12), 1727–1738.
- Capitanio, F. A., Morra, G., & Goes, S., 2009. Dynamics of plate bending at the trench and slab-plate coupling, *Geochemistry, Geophysics, Geosystems*, 10(4).
- Cathles, L. M., 2015. Viscosity of the Earth's mantle.
- Christensen, U. R. & Yuen, D. A., 1985. Layered convection induced by phase transitions, *Journal of Geophysical Research: Solid Earth*, 90(B12), 10291–10300.
- Čížková, H. & Bina, C. R., 2019. Linked influences on slab stagnation: Interplay between lower mantle viscosity structure, phase transitions, and plate coupling, *Earth and Planetary Science Letters*, 509, 88–99.
- Coltice, N., Blessing, S., Giering, R., & Tackley, P., 2023. Sensitivity analysis of global kinematics on mantle structure using automatically generated adjoint thermochemical convection codes.
- Conrad, C. P. & Hager, B. H., 1999. Effects of plate bending and fault strength at subduction zones on plate dynamics, *Journal of Geophysical Research: Solid Earth*, 104(B8), 17551–17571.
- Conrad, C. P. & Husson, L., 2009. Influence of dynamic topography on sea level and its rate of change, *Lithosphere*, 1(2), 110–120.
- Conrad, C. P. & Lithgow-Bertelloni, C., 2002. How mantle slabs drive plate tectonics, *Science*, 298(5591), 207–209.
- Cui, F., Li, Z.-H., & Fu, H.-Y., 2024. Quantitative evaluation of mantle flow traction on overlying tectonic plate: linear versus power-law mantle rheology, *Geophysical Journal International*, 239(2), 1063–1079.
- Davies, D. R., Valentine, A., Kramer, S. C., Rawlinson, N., Hoggard, M., Eakin, C., & Wilson, C., 2019. Earth's multi-scale topographic response to global mantle flow, *Nature Geoscience*, 12(10), 845–850.
- Fei, H., Ballmer, M. D., Faul, U., Walte, N., Cao, W., & Katsura, T., 2023. Variation in bridgmanite grain size accounts for the mid-mantle viscosity jump, *Nature*, 620(7975), 794–799.
- Flament, N., Gurnis, M., & Müller, R. D., 2013. A review of observations and models of dynamic topography, *Lithosphere*, 5(2), 189–210.
- Forté, A., Peltier, W., & Dziewonski, A., 1991. Inferences of

- mantle viscosity from tectonic plate velocities, *Geophysical Research Letters*, 18(9), 1747–1750.
- Gerya, T., 2019. Introduction to numerical geodynamic modelling, Cambridge University Press.
- Ghelichkhan, S., Gibson, A., Davies, D. R., Kramer, S. C., & Ham, D. A., 2024. Automatic adjoint-based inversion schemes for geodynamics: reconstructing the evolution of earth’s mantle in space and time, *Geoscientific Model Development*, 17(13), 5057–5086.
- Goes, S., Agrusta, R., van Hunen, J., & Garel, F., 2017. Subduction-transition zone interaction: A review, *Geosphere*, 13(3), 644–664.
- Hager, B. & Richards, M., 1989. Long-wavelength variations in earth’s geoid: physical models and dynamical implications, *Philosophical Transactions of the Royal Society of London. Series A, Mathematical and Physical Sciences*, 328(1599), 309–327.
- Hager, B. H., 1984. Subducted slabs and the Geoid: Constraints on mantle rheology and flow, *J. Geophys. Res.*, 89, 6003–6015.
- Hirth, G. & Kohlstedt, D., 2003. Rheology of the upper mantle and the mantle wedge: A view from the experimentalists, *Geophysical monograph-american geophysical union*, 138, 83–106.
- Hoggard, M., White, N., & Al-Attar, D., 2016. Global dynamic topography observations reveal limited influence of large-scale mantle flow, *Nature Geoscience*, 9(6), 456–463.
- Horbach, A., Bunge, H., & Oeser, J., 2014. The adjoint method in geodynamics: derivation from a general operator formulation and application to the initial condition problem in a high resolution mantle circulation model, *Int J Geomath*, pp. 1–32.
- Hu, J., Gurnis, M., Rudi, J., Stadler, G., & Müller, R. D., 2022. Dynamics of the abrupt change in Pacific Plate motion around 50 million years ago, *Nature Geoscience*, 15(1), 74–78.
- Hu, J., Rudi, J., Gurnis, M., & Stadler, G., 2024. Constraining earth’s nonlinear mantle viscosity using plate-boundary resolving global inversions, *Proceedings of the National Academy of Sciences*, 121(28), e2318706121.
- Karato, S., 2008. Deformation of Earth materials : An introduction to the rheology of solid Earth, Cambridge University Press.
- Karato, S. & Wu, P., 1993. Rheology of the upper mantle: A synthesis, *Science*, 260(5109), 771–778.
- Korenaga, J. & Karato, S.-I., 2008. A new analysis of experimental data on olivine rheology, *Journal of Geophysical Research: Solid Earth*, 113(B2).
- Kronbichler, M., Heister, T., & Bangerth, W., 2012. High accuracy mantle convection simulation through modern numerical methods, *Geophysical Journal International*, 191(1), 12–29.
- LeCun, Y., Touresky, D., Hinton, G., & Sejnowski, T., 1988. A theoretical framework for back-propagation, in *Proceedings of the 1988 connectionist models summer school*, vol. 1, pp. 21–28.
- Leng, W. & Zhong, S., 2010. Constraints on viscous dissipation of plate bending from compressible mantle convection, *Earth and Planetary Science Letters*, 297(1-2), 154–164.
- Li, K., Hu, J., Li, Y., Zhou, H., & Zhang, H., 2024a. Slab segmentation and stacking in mantle transition zone controls disparate surface and lower mantle subducting rates and complex slab morphology, *Geophysical Research Letters*, 51(17), e2024GL110202.
- Li, Y., Liu, L., Li, S., Peng, D., Cao, Z., & Li, X., 2024b. Cenozoic india-asia collision driven by mantle dragging the cratonic root, *Nature Communications*, 15(1), 6674.
- Li, Z.-H., Gerya, T., & Connolly, J. A., 2019. Variability of subducting slab morphologies in the mantle transition zone: Insight from petrological-thermomechanical modeling, *Earth-Science Reviews*, 196, 102874.
- Lithgow-Bertelloni, C. & Richards, M. A., 1998. The dynamics of cenozoic and mesozoic plate motions, *Reviews of Geophysics*, 36(1), 27–78.
- Liu, D. C. & Nocedal, J., 1989. On the limited memory bfgs method for large scale optimization, *Mathematical programming*, 45(1), 503–528.
- Liu, F., Li, H., Zou, G., & Li, J., 2025. Automatic differentiation-based full waveform inversion with flexible workflows, *Journal of Geophysical Research: Machine Learning and Computation*, 2(1), e2024JH000542.
- Liu, X. & Zhong, S., 2015. The long-wavelength geoid from three-dimensional spherical models of thermal and thermochemical mantle convection, *Journal of Geophysical Research: Solid Earth*, 120(6), 4572–4596.
- Mansour, J., Giordani, J., Moresi, L., Beucher, R., Kaluza, O., Velic, M., Farrington, R., Quenette, S., & Beall, A., 2020. Underworld2: Python geodynamics modelling for desktop, hpc and cloud, *Journal of Open Source Software*, 5(47), 1797.
- McNamara, A. K. & Zhong, S., 2005. Thermochemical structures beneath africa and the pacific ocean, *Nature*, 437(7062), 1136–1139.
- Mitrovica, J. X. & Forte, A. M., 2004. A new inference of mantle viscosity based upon joint inversion of convection and glacial isostatic adjustment data, *Earth and Planetary Science Letters*, 225(1–2), 177 – 189.
- Paszke, A., Gross, S., Chintala, S., Chanan, G., Yang, E., DeVito, Z., Lin, Z., Desmaison, A., Antiga, L., & Lerer, A., 2017. Automatic differentiation in pytorch.
- Plessix, R.-E., 2006. A review of the adjoint-state method for computing the gradient of a functional with geophysical applications, *Geophysical Journal International*, 167(2), 495–503.
- Raissi, M., Perdikaris, P., & Karniadakis, G. E., 2019. Physics-informed neural networks: A deep learning framework for solving forward and inverse problems involving nonlinear partial differential equations, *Journal of Computational physics*, 378, 686–707.
- Rall, L. B., 1981. Automatic differentiation: Techniques and applications, Springer.
- Ranalli, G., 1995. Rheology of the Earth, Springer Science & Business Media.
- Ratnaswamy, V., Stadler, G., & Gurnis, M., 2015. Adjoint-based estimation of plate coupling in a non-linear mantle flow model: theory and examples, *Geophysical Journal International*, 202(2), 768–786.
- Reuber, G. S., Holbach, L., Popov, A. A., Hanke, M., & Kaus, B. J. P., 2020. Inferring rheology and geometry of subsurface structures by adjoint-based inversion of principal stress directions, *Geophysical Journal International*, 223(2), 851–861.

- Rudi, J., Gurnis, M., & Stadler, G., 2022. Simultaneous inference of plate boundary stresses and mantle rheology using adjoints: large-scale 2-d models, *Geophysical Journal International*, 231(1), 597–614.
- Rudolph, M. L., Lekić, V., & Lithgow-Bertelloni, C., 2015. Viscosity jump in earth’s mid-mantle, *Science*, 350(6266), 1349–1352.
- Sambridge, M., Rickwood, P., Rawlinson, N., & Sommacal, S., 2007. Automatic differentiation in geophysical inverse problems, *Geophysical Journal International*, 170(1), 1–8.
- Schellart, W. P., 2009. Evolution of the slab bending radius and the bending dissipation in three-dimensional subduction models with a variable slab to upper mantle viscosity ratio, *Earth and Planetary Science Letters*, 288(1-2), 309–319.
- Schmalholz, S. M., 2011. A simple analytical solution for slab detachment, *Earth and Planetary Science Letters*, 304(1-2), 45–54.
- Shi, Z., Mitchell, R. N., Li, Y., Wan, B., Chen, L., Peng, P., Zhao, L., Liu, L., & Zhu, R., 2024. Sluggish thermochemical basal mantle structures support their long-lived stability, *Nature Communications*, 15(1), 10000.
- Snoek, J., Larochele, H., & Adams, R. P., 2012. Practical bayesian optimization of machine learning algorithms, *Advances in neural information processing systems*, 25.
- Sobolev, S. V. & Brown, M., 2019. Surface erosion events controlled the evolution of plate tectonics on earth, *Nature*, 570(7759), 52–57.
- Stadler, G., Gurnis, M., Burstedde, C., Wilcox, L. C., Alisic, L., & Ghattas, O., 2010. The dynamics of plate tectonics and mantle flow: From local to global scales, *Science*, 329(5995), 1033–1038.
- Steinberger, B., 2007. Effects of latent heat release at phase boundaries on flow in the earth’s mantle, phase boundary topography and dynamic topography at the earth’s surface, *Physics of the Earth and Planetary Interiors*, 164(1-2), 2–20.
- Steinberger, B. & Calderwood, A. R., 2006. Models of large-scale viscous flow in the earth’s mantle with constraints from mineral physics and surface observations, *Geophysical Journal International*, 167(3), 1461–1481.
- Torsvik, T. H., Smethurst, M. A., Burke, K., & Steinberger, B., 2008. Long term stability in deep mantle structure: Evidence from the ~ 300 ma skagerrak-centered large igneous province (the sclip), *Earth and Planetary Science Letters*, 267(3-4), 444–452.
- Wang, Y., Lai, C.-Y., Prior, D. J., & Cowen-Breen, C., 2025. Deep learning the flow law of antarctic ice shelves, *Science*, 387(6739), 1219–1224.
- Worthen, J., Stadler, G., Petra, N., Gurnis, M., & Ghattas, O., 2014. Towards adjoint-based inversion for rheological parameters in nonlinear viscous mantle flow, *Physics of the Earth and Planetary Interiors*, 234, 23–34.
- Wu, B., Conrad, C. P., Heuret, A., Lithgow-Bertelloni, C., & Lallemand, S., 2008. Reconciling strong slab pull and weak plate bending: The plate motion constraint on the strength of mantle slabs, *Earth and Planetary Science Letters*, 272(1-2), 412–421.
- Yang, T. & Gurnis, M., 2016. Dynamic topography, gravity and the role of lateral viscosity variations from inversion of global mantle flow, *Geophysical Journal International*, 207(2), 1186–1202.
- Yang, T., Moresi, L., Müller, R. D., & Gurnis, M., 2017. Oceanic residual topography agrees with mantle flow predictions at long wavelengths, *Geophysical Research Letters*, 44(21), 10–896.
- Zhang, J., Hu, J., & Sun, D., 2024. Segregation of a thermochemical anomaly and coalescence with a large low-velocity province, *Nature Geoscience*, pp. 1–8.
- Zhong, S., 1996. Analytic solutions for stokes’ flow with lateral variations in viscosity, *Geophysical Journal International*, 124(1), 18–28.
- Zhou, H., Hu, J., Dal Zilio, L., Tang, M., Li, K., & Hu, X., 2024. India–eurasia convergence speed-up by passive-margin sediment subduction, *Nature*, 635(8037), 114–120.
- Zhu, W., Xu, K., Darve, E., & Beroza, G. C., 2021. A general approach to seismic inversion with automatic differentiation, *Computers & Geosciences*, 151, 104751.
- Zhu, W., Xu, K., Darve, E., Biondi, B., & Beroza, G. C., 2022. Integrating deep neural networks with full-waveform inversion: Reparameterization, regularization, and uncertainty quantification, *Geophysics*, 87(1), R93–R109.

## APPENDIX A: BENCHMARK

To validate the accuracy and correctness of the forward computations, we provide three benchmark tests: Solcx, SolKz(Mansour et al., 2020), and Slab Detachment((Schmalholz, 2011),(Kronbichler et al., 2012)). The Solcx benchmark demonstrates the model’s capability in dealing with sharp viscosity contrast, while the SolKz benchmark features a more gentle viscosity gradient but a more complex density variation. The Slab Detachment is used to test the model’s performance in dealing with nonlinear rheology.

### A1 Solcx

The Solcx analytical solution is used as a benchmark. The Solcx solution features a sharp viscosity contrast and a sinusoidal density distribution, providing stringent conditions for testing the system’s accuracy ((Zhong, 1996)). The viscosity field  $\eta$  exhibits a discontinuity at the position  $x_c$ , and its expression is given as:

$$\eta = \begin{cases} \eta_A & \text{while } x < x_c, \\ \eta_B & \text{while } x \geq x_c \end{cases} \quad (\text{A.1})$$

Here,  $\eta_A$  represents the viscosity of region A,  $\eta_B$  represents the viscosity of region B, and  $x_c$  denotes the location of the viscosity contrast. In this model, the parameters are set as  $\eta_A = 1$ ,  $\eta_B = 10^5$ , with the viscosity contrast occurring at  $x_c = 0.75$ . The viscosity field is shown in Fig.A1b.

The body force field  $f$  is defined using a trigonometric distribution in the form of sine and cosine functions, expressed as:

$$f = -\cos(\pi x) \sin(n_z \pi y), \quad (\text{A.2})$$

Here,  $x, y$  represent the normalized spatial coordinates with values ranging from  $[0, 1]$ , and  $n_z$  denotes the wavenumber parameter, which is set to  $n_z = 1$  in this study. The trigonometric distribution of the density field effectively simulates

complex volumetric force distributions, as illustrated in Figure.A1a.

The boundary conditions are defined as free-slip on all four sides, meaning that the velocity component perpendicular to the boundary is zero, while the parallel component is unconstrained. These boundary conditions ensure zero shear stress on the boundaries, which is consistent with typical geodynamic settings.

Velocity error distribution between the numerical solution and the analytical solution is presented (Figure.A1d). The error is predominantly concentrated near the viscosity jump location ( $x = x_c$ ), with a peak value of approximately  $1.2 \times 10^{-4}$ . In other regions, the error is minimal and more uniformly distributed. This indicates that the numerical model maintains high accuracy when handling viscosity discontinuities, with the primary source of error arising from interpolation and numerical approximation in the viscosity jump.

The root-mean-square relative error provides a measure of the relative error between the analytical solution and the numerical solution (eq. (A.3)).

$$vrms = \frac{\sum ((v_x - v_x^{true})^2 + (v_y - v_y^{true})^2)^{1/2}}{\sum ((v_x^{true})^2 + (v_y^{true})^2)^{1/2}} \quad (A.3)$$

The results are shown in Fig.A1A. As the resolution increases, the error shows a clear decreasing trend. When the resolution is increased from  $64 \times 64$  to  $512 \times 512$ , the error decreases from 4.7% to 0.5%. This declining trend in the error demonstrates the correctness of our numerical method.

## A2 SolKz

The SolKz solution features viscosity that varies exponentially with depth  $z$  and a trigonometric volumetric force, allowing for the evaluation of numerical models' performance under high-gradient viscosity fields and complex driving forces (Mansour et al., 2020).

In the SolKz solution, the viscosity  $\eta$  increases exponentially with depth  $z$ , as expressed by:

$$\eta(z) = \eta_0 \exp(Bz) \quad (A.4)$$

where  $\eta_0$  represents the reference viscosity, and  $B$  is a parameter controlling the rate of viscosity variation with depth. Here, the parameter  $B = 2.3$  is chosen to ensure a significant variation in viscosity with depth, which helps test the numerical model's accuracy under high-gradient viscosity conditions. The viscosity field distribution is shown in Fig.A2a.

The body force term adopts a trigonometric form, expressed as:

$$f = \sigma_0 \cos(n_x \pi x) \sin(n_z \pi z) \quad (A.5)$$

where  $\sigma_0$  represents the perturbation intensity factor, while  $n_x$  and  $n_z$  denote the wavenumber parameters in the  $x$ - and  $z$ -directions, respectively. The parameters are set as follows:  $\sigma_0 = 1.0$ ,  $n_x = 3$ , and  $n_z = 2.0$ .

The resulting density field distribution under this setup is shown in Fig.A2b, illustrating the periodic variation of density in both the  $x$ - and  $z$ -directions. The four boundaries are set as free-slip, ensuring that the velocity component

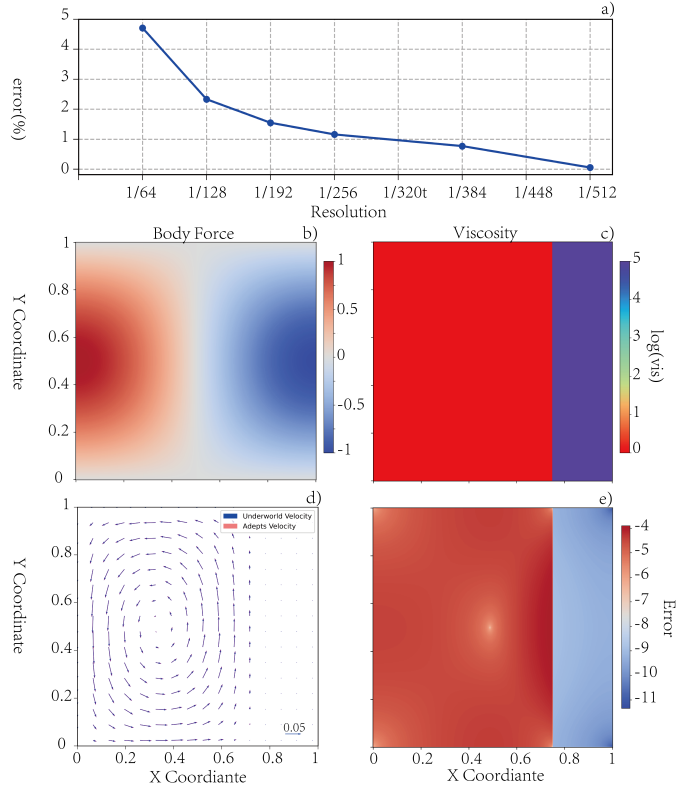


Figure A1. The SolCx benchmark results. (a) shows the decreasing relative error with increasing resolution (from  $1/64$  to  $1/512$ ), highlighting improved accuracy. (b) depicts the body force distribution, with red indicating high-body force regions and blue showing low-body force regions. (c) displays the viscosity distribution, where red represents high-viscosity areas and blue denotes low-viscosity areas. (d) compares velocity vector fields of the analytical solution (blue arrows) and numerical solution (red arrows) with a model resolution of  $512 \times 512$ , showing strong agreement. (e) visualizes the velocity error  $\log_{10}(\text{error})$ , with red marking larger errors and blue indicating smaller ones, primarily concentrated in high-gradient regions.

perpendicular to the boundary is zero, while the parallel component is unconstrained.

The relative velocity error of the numerical model is mainly concentrated in regions of high density and low viscosity, as expected (Fig.A2d and Fig.A2e). The peak error is small ( $1.4 \times 10^{-5}$ ), demonstrating high accuracy in high-viscosity gradient regions.

The trend of error variation with resolution is illustrated in Fig.A2a. As the resolution increases from  $64 \times 64$  to  $512 \times 512$ , the error, computed using Equation (A.3), decreases from 1.4% to 0.1%. This convergence demonstrates that the numerical model gradually approaches the SolKz exact solution under high-resolution conditions, showcasing excellent stability and convergence.

## A3 Slab detachment

This benchmark test is based on the setup by Schmalholz (2011) and the implementation in Underworld2 (Mansour et al., 2020). The computational domain is a rectangular

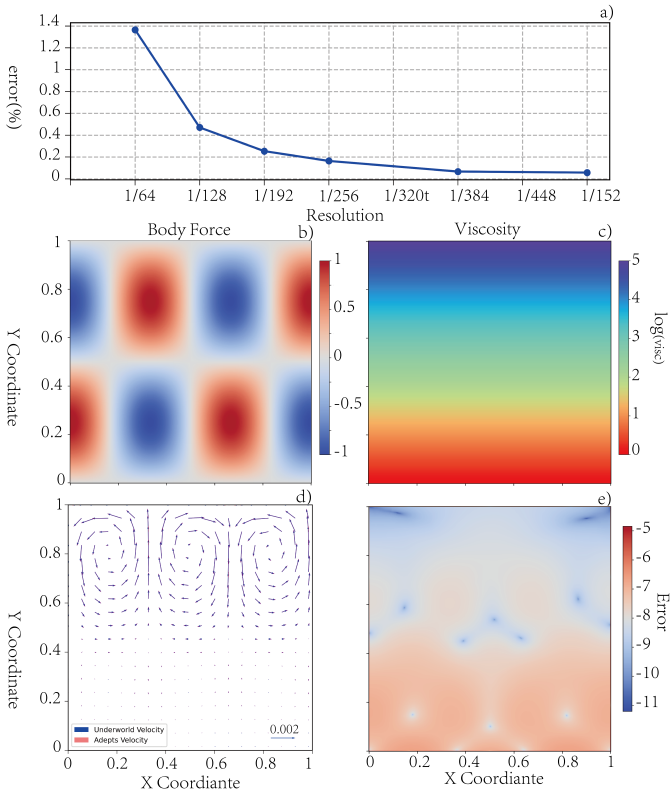


Figure A2. The SolKz benchmark results. (a) shows decreasing relative error with higher resolution, indicating improved accuracy. (b) illustrates the periodic body force distribution. (c) depicts the viscosity distribution with a vertical gradient. (d) compares velocity vector fields from analytical and numerical solutions. (e) visualizes velocity error. Symbols and legends are the same as Fig. A1.

region with a dimension of  $1000 \text{ km} \times 660 \text{ km}$ , and all four boundaries are assigned free-slip boundary conditions.

The computational domain contains two materials: the lithosphere and the mantle, as shown in Fig.A3b. The lithosphere has a thickness of 80 km and is located at the top of the domain, including a subducting slab that extends vertically into the mantle to a depth of approximately 250 km. The lithosphere has a density of  $\rho_s = 3300 \text{ kg/m}^3$ , and a power-law rheology. The effective viscosity  $\eta_{\text{eff}}$  depends on the square root of the second invariant of the strain rate  $\dot{\epsilon}$ , and is expressed as:

$$\eta_{\text{eff}} = \eta_0 \dot{\epsilon}^{1/n-1}, \quad (\text{A.6})$$

Here,  $n = 4$  and  $\eta_0 = 4.75 \times 10^{11} \text{ Pa} \cdot \text{s}^{\frac{1}{n}}$ .

The mantle occupies the remainder of the computational domain, with a constant viscosity of  $\eta_m = 1 \times 10^{21} \text{ Pa} \cdot \text{s}$  and a density of  $\rho_m = 3150 \text{ kg/m}^3$ . To ensure numerical stability, the viscosity in the model is constrained within the range of  $1 \times 10^{21} \text{ Pa} \cdot \text{s}$  to  $1 \times 10^{25} \text{ Pa} \cdot \text{s}$ .

The velocity vector comparison between the true velocity field and the predicted velocity field shows a high level of consistency in the overall structure of the two velocity fields, especially in the mantle circulation region and near the subduction zone (Fig.A3b). The differences in velocity vector direction and magnitude are minimal, with slight deviations occurring at the lithosphere-mantle interface, which can be

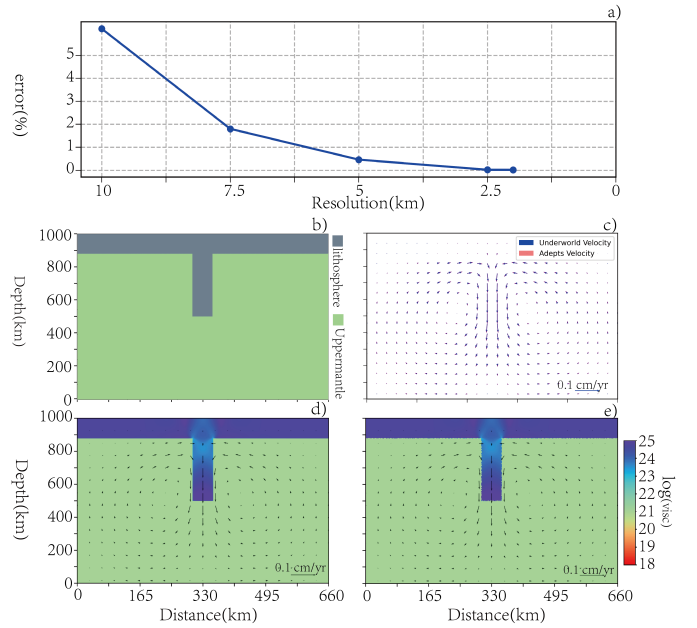


Figure A3. The slab detachment benchmark, comparing the results from Underworld2 and this study. (a) shows a significant reduction in error as resolution improves from 10 km to 2.5 km, indicating enhanced accuracy. (b) illustrates the material field, with gray representing the lithosphere and green denoting the upper mantle, showing geological unit geometry. (c) compares velocity fields of models with resolution of 1.25 km from Underworld2 (blue arrows) and this study (red arrows), showing strong agreement. (d) and (e) display viscosity and velocity fields from Underworld2 and this study, respectively, with color gradients indicating viscosity variations and overlaid vectors representing flow dynamics. Both models show consistent results, effectively capturing slab detachment features.

attributed to numerical interpolation errors in high-gradient regions. Moreover, as the model resolution improves, the overall velocity root-mean-square (vrms) error is further reduced (Fig.A3A).

The benchmark results demonstrate that our forward modeling algorithm can accurately capture the overall distribution and local details of the velocity field under nonlinear rheological properties. The numerical errors are minimal and show a high level of consistency with the model results from Underworld2.